Main Manuscript for

Nearly three decades of laser altimetry reveal strong regional contrasts and glacier-driven ice losses in Greenland

Hui Gao[a], Beata M Csatho[a], Anton F Schenk[a], Michael J Croteau[b], Surendra Adhikari[c], Ivan Parmuzin[a], Nicole-Jeanne Schlegel[d], Max Brils[e], Michiel R. van den Broeke[f], Denis Felikson[g], Bryant Loomis[b], Brooke Medley[g], Brice Noël[h], Sophie Nowicki[a,i], and Kristin Poinar[a,i]

[a]Department of Earth Sciences, University at Buffalo, Buffalo, NY 14260; [b]Geodesy and Geophysics Laboratory, NASA Goddard Space Flight Center, Greenbelt, MD 20771; [c]Jet Propulsion Laboratory, California Institute of Technology, Pasadena, CA 91109; [d]NOAA/OAR Geophysical Fluid Dynamics Laboratory, Princeton, NJ 08540; [e]School of Geography and Environmental Sciences, Northumbria University, Newcastle upon Tyne, UK; [f]Institute for Marine and Atmospheric Research Utrecht, Utrecht University, Utrecht, Netherlands; [g]Cryospheric Sciences Laboratory, NASA Goddard Space Flight Center, Greenbelt, MD 20771; [h]Laboratory of Climatology, Department of Geography, SPHERES research unit, University of Liège, Liège, Belgium; [i]RENEW Institute, University at Buffalo, Buffalo, NY 14260

*Hui Gao

Email: hgao7@buffalo.edu

Author Contributions: B.M.C., H.G., S.N., and K.P. conceptualized research; B.M.C. and H.G. designed research; H.G., B.M.C., and M.J.C. performed research; A.F.S., M.J.C., S.A., I.P., N.S., M.B., M.R.v.d.B., D.F., B.M., B.L., and B.N. contributed new data; H.G., B.M.C., M.J.C., and S.A. analyzed data; and H.G., B.M.C., and M.J.C. wrote the original draft of the paper; all authors contributed to reviewing and editing the final paper.

Competing Interest Statement: The authors declare no competing interest.

Preprint Servers: EarthArXiv, CC BY 4.0

Classification: Physical Sciences, Earth, Atmospheric, and Planetary Sciences

Keywords: Greenland Ice Sheet, laser altimetry, mass change, ice dynamics, sea level

This PDF file includes:

Main Text
Figures 1 to 6
Tables 1

Abstract

The Greenland Ice Sheet, a major contributor to sea-level rise, loses mass through complex processes that are not fully understood. Laser altimetry provides direct and accurate measurements of ice sheet surface elevation. Here, we present the first continuous, laser altimetry-based annual reconstruction of Greenland Ice Sheet mass change from 1994 to 2020 at 1 km horizontal resolution. Our novel approach fuses NASA's multi-mission laser altimetry records and isolates dynamic ice thickness change. We estimate an average mass loss of 191 ± 6 Gt/yr, with the most intense thinning concentrated in western and southeastern regions, driven by enhanced surface melt and dynamic ice mass loss. Despite challenges in partitioning surface and dynamic components, we find a robust temporal evolution of dynamic thinning that reveals diverse thinning patterns across tidewater glaciers. This high-resolution reconstruction provides a crucial, observation-based benchmark for model calibration and evaluation that illuminates the complex drivers of ice sheet mass change across spatial and temporal scales.

Significance Statement

The Greenland Ice Sheet is losing mass rapidly, yet its strong regional variability remains difficult to resolve at high spatial resolution. We present the first continuous, annual reconstruction of Greenland Ice Sheet mass change at a 1 km resolution from 1994 to 2020 using multi-mission laser altimetry, with uncertainties in firn processes quantified. This reconstruction highlights severe mass loss in the Northwest and Southeast, contrasting with much lower rates in the North and Northeast. Partitioning atmospheric and dynamic contributions uncovers distinct regional mass change mechanisms and the highly diverse behaviors of individual tidewater glaciers. Ultimately, this observation-based record provides a critical benchmark for improving ice sheet models and projecting future sea-level rise.

Main Text

Introduction

The Greenland Ice Sheet (GrIS) has accounted for approximately a quarter of the observed global mean sea level rise since 1900 and is projected to continue losing ice throughout the 21st century (1, 2). Ice is primarily lost through increased surface melt and ice discharge into the ocean through calving and submarine melting at marine-terminating outlet glaciers, also known as tidewater glaciers (3). Different regions of the ice sheet are subject to different climatic conditions and local geometric environments and may have different responses and sensitivities to changes in atmospheric and oceanic conditions. For example, northern and northeastern Greenland are generally cold and dry and are characterized by a few large tidewater glaciers and ice streams with large floating ice tongues (4). In contrast, the southeastern region is mountainous, has a high amount and variability of precipitation, and contains many tidewater glaciers but none with significant floating portions (5). The tidewater glaciers in the southeast are close to the warm and salty Atlantic Waters (AW), which originate in the North Atlantic Ocean (6). On the west coast, numerous tidewater glaciers in the northwest and central west Greenland drain the ice into the ocean, while the ice sheet in the southwestern region is mostly land-terminating (6). Meters-thick layers of ice, known as ice slabs, have been forming and expanding in the percolation zone of western and northern Greenland in response to enhanced meltwater refreezing (7). This spatial diversity in ice flow and mass change processes implies that a regional-scale assessment of ice sheet mass change, including its major components, is critical for understanding ice-climate interactions. Such an assessment is needed to enhance the calibration and evaluation of ice-sheet models to help reduce uncertainties in projecting the future contribution of the Greenland Ice Sheet to sea-level rise (8, 9).

Reconstructions of contemporary ice-sheet mass change are categorized into three groups: altimetry, gravimetry, and the input-output method (10). Altimetry measures surface elevation change. The small footprint size (less than 100 m in diameter) and high vertical measurement accuracy (< 0.2 m measurement error) of laser altimetry enable the evaluation of the spatial variability of mass change, especially on the rapidly changing tidewater glaciers (11). Elevations measured by radar altimetry have a higher uncertainty because of the radar penetration into ice and snow and the much larger footprint size (12). To convert surface elevation change to mass change, we correct for the vertical land motion from the viscoelastic deformation of the Earth's crust and underlying mantle and changes in the densities of firn layers (formed from snow accumulating and compacting). Gravimetry measures variations in the Earth's gravity field caused by mass redistribution (13). The time-resolved satellite gravimetry measurements from the Gravity Recovery and Climate Experiment (GRACE) have greatly enhanced our understanding of mass transport processes within the Earth system, particularly those related to the hydrosphere and cryosphere (13, 14). Mass change reconstructions using GRACE (2002–2017) and GRACE Follow-on (FO, 2018–present) provide monthly temporal resolution but are limited by their low spatial resolution of ~300 km in Greenland (15). The input-output method calculates mass change as the difference between the input from Surface Mass Balance (SMB, net mass change at the ice sheet surface due to atmospheric processes) and output from ice discharge (16). While ice sheet-wide observation from altimetry and gravimetry records spans the satellite era (e.g., post-1990s), the input-output method can reconstruct mass changes over much longer periods (e.g., 1972-present or earlier) by leveraging modeled SMB and ice thickness and velocity at flux gates (17, 18). The Ice Sheet Mass Balance Intercomparison Exercise (IMBIE) attempts to reconcile ice sheet mass change estimations from these three methods (10, 19). This reconciliation is done at the ice sheet scale and has not yet been focused down to the drainage basin scale in Greenland.

Since 1993, NASA has been observing the Greenland Ice Sheet using airborne and satellite laser altimetry (20–22). The two satellite missions, ICESat (Ice, Cloud and land Elevation Satellite, 2003–2009) and ICESat-2 (2018–present), have been successfully used for ice sheet mass change reconstruction at a spatial resolution as high as 5 km (23, 24). Two additional airborne missions extended the timeline to 1993–present, with the Airborne Ice Mapping (AIM, 1993–2008) mission providing an initial estimate of GrIS mass changes and the Operation Ice Bridge mission (OIB, 2009–2021, last Greenland land ice flight in 2019) bridging the ICESat and ICESat-2 satellite missions (20). Both airborne missions had irregular and relatively sparse temporal and spatial sampling due to their prescribed focus on repeat surveys of major outlet glaciers (Fig. S1). As a result, the use of airborne surveys is often limited to validating satellite altimetry measurements of surface elevation change (25) or combining with satellite altimetry to improve mass change reconstructions near the ice sheet margin (26). Here, we present the first continuous annually resolved laser altimetry-based reconstruction of the GrIS mass change between September 1, 1994, and August 31, 2020, at 1 km horizontal resolution (Fig. 1). This extends the nineteen-year 1993–2012 record of (11) to 26 years.

Our mass change reconstruction uses the complete surface elevation change time series at over 54,000 locations (Fig. S2), including most ICESat ground tracks, from the Surface Elevation Reconstruction And Change detection (SERAC) method (27). SERAC fuses NASA's airborne and satellite laser altimetry measurements between 1993 and 2022 and digital elevation models (DEMs) from stereo aerial photographs between 1978 and 1987 (11, 27, 28). Unlike previous studies that estimate firn density or corrected for changes in firn air content to convert volume change to mass change (11, 24, 29, 30), we directly remove firn height change caused by surface processes from the surface elevation change time series. The firn height change estimates consist of changes due to SMB anomalies and firn air content (FAC) change. After the viscoelastic solid earth vertical land motion (Fig. S3) (31, 32) is also removed, the residuals represent the ice thickness change due to ice dynamics from perturbations to ice flow (Fig. S4). The relatively smooth behavior of the dynamic ice thickness change time series allowed a robust estimation of its annual change despite the irregularly spaced airborne data acquisitions (Fig. S2). Here, we obtained three mass change reconstructions that are partitioned into surface and dynamic mass change using three different firn height change and surface mass balance datasets from firn densification models (FDMs): IMAU-FDM v1.2G forced by RACMO2.3p2 (33, 34), GSFC-FDM v1.2.1 forced by MERRA-2 (35, 36), and GEMB v1.0 forced by corrected ERA5 (37).

We use the average of our three reconstructions as our final altimetry-based mass change estimation. Despite using only three FDMs, the standard deviation of our three reconstructions provides an initial estimate of the mass change uncertainties arising from uncertainties in firn air content and height change estimates, especially biases that are poorly understood. The mass change uncertainties represented by the standard deviation of the three reconstructions are of the same magnitude as uncertainties estimated from formal error propagation (SI Text). Following (17), we divide the Greenland ice sheet into seven drainage basins: northeast (NE), central east (CE), southeast (SE), southwest (SW), central west (CW), northwest (NW), and north (NO). We analyze mass change patterns at the ice sheet, drainage basin, and individual glacier scales and compare our mass change estimates with GRACE (15, 38). All annual changes are reconstructed for balance years, with 1995, for example, referring to September 1, 1994, to August 31, 1995.

Results

Spatiotemporal variation of ice mass change

Between 1994 and 2020, we estimated an average ice mass loss rate of 191 ± 6 Gt/year from the Greenland Ice Sheet (Fig. 1 and Table 1). Our results agree well with the IMBIE3 estimate of 179 ± 16 Gt/year for the same period (19) and other independent studies (Table S1) (11, 17, 24, 29, 39). When partitioning the total mass change into changes due to surface processes (SMB anomaly) and ice dynamics (dynamic mass change), we found widespread negative SMB anomalies in the ablation zone and dynamic thinning of tidewater glaciers that extended well above the average 1994–2020 equilibrium line altitude (ELA, where the net ice accumulation is zero, black dashed line in Fig. 1) (Figs. 1 and 2). Our surface elevation change reconstruction reveals that although the elevation of 48% of the ice sheet area increased between 1994 and 2020, the cumulative increase across most of these areas was less than 2 m (Fig. S5). In contrast, the elevation-decreasing region exhibited a much larger change, with 11% of the ice sheet undergoing a cumulative decrease in excess of 10 m.

The ice sheet had record mass losses of more than 420 Gt/year in 2012 and 2019 (Fig. 3). The large interannual variability in our results (for example, see the contrasting mass change of 1995 and 1996 in Fig. S6) stems primarily from interannual variability in SMB (Fig. 3). In comparison, dynamic mass change varies at a longer timescale (Fig. 3). When we divide the mass change into five-year periods, we find that the Greenland Ice Sheet was losing mass at an increasing rate, peaking at 291 ± 19 Gt/year between 2010 and 2015, after which the mass loss rate decreased to 209 ± 11 Gt/year (Fig. 2 and Table 1). Comparing the mass changes from the well-sampled ICESat years of 2003–2009 (194 ± 17 Gt/year) to the more recent period of 2014–2020 (212 ± 11 Gt/year), we found widespread mass loss increases in western Greenland, especially the southwest (Fig. 3 middle map). Meanwhile, we also found increased mass loss near the termini of many tidewater glaciers, especially in the NW, NO, and NE, and further upstream of large outlet glaciers, such as Jakobshavn Isbrae (glacier 5 in Fig. 3). These increases are partially balanced by the reduced dynamic thinning near the termini of some tidewater glaciers, such as Jakobshavn Isbrae and Kangerlussuaq (glaciers 5 and 7 in Fig. 3, respectively) and decreased surface mass loss in eastern Greenland, especially in the CE and SE (Fig. S7).

The uncertainties of the 1994–2020 total mass change estimations, expressed as the standard deviation of our three reconstructions, mainly reflect the spread in firn air content change from the three FDMs. Between 1994 and 2020, the standard deviation of annual total mass change rates averaged 18 Gt/year, ranging from 5 Gt/year in 2005 to 50 Gt/year in 2012 (Fig. 3). Spatially, the most significant differences of the three 1994–2020 mass change estimates are found in narrow regions, parallel with the ice sheet boundary in southeast and south Greenland and near the ELA in northern and western Greenland (Fig. 1F). These regions all host extensive firn aquifers and ice slabs that can complicate local firn densification (7)

While calculating the drainage basin mass changes, we took the intersection of the drainage basin outline from (17) with the floating-tongue-corrected CCI (ESA Climate Change Initiative) ice sheet mask (release 2.0) (40, 41). Over the period 1994–2020, all drainage basins lost mass but did so at very different rates (Fig. 3 and Table 1). The NW underwent the highest average mass loss at a rate of 50 ± 3 Gt/year, increasing from 8 ± 1 Gt/year between 1995 and 2000 to 80 ± 5/year between 2010 and 2015 (Table 1). The SE ranked second, with an average mass loss rate of 45 ± 1 Gt/year, peaking at 58 ± 3 Gt/year between 2005 and 2010. The CE maintained a high mass loss rate averaging 32 ± 4 Gt/year. The SW has been losing mass at an increasing rate, averaging 26 ± 4 Gt/year. The CW has been losing ice at a similar rate of 26 ± 4 Gt/year, increasing since the 1990s and peaking between 2010 and 2015. The NO has been losing ice at a moderate rate of 9 ± 1 Gt/year, which has been increasing in recent years. The NE showed the lowest mass loss rate of all basins at 3 ± 3 Gt/year.

Comparison with mass change from GRACE

We compared our total mass change reconstructions with the 1-arc-degree NASA Goddard Space Flight Center GRACE and GRACE-FO mascon solutions (Fig. 4A), hereafter collectively referred to as GRACE, at the ice sheet and drainage basin scales (15, 38). To compare with our ice sheet-only mass change reconstructions, we replaced the Glacial Isostatic Adjustment (GIA) model in the altimetry-based reconstructions with ICE_6G-D used in the GRACE mascon solution (42) and removed mass change of peripheral glaciers and ice caps (GICs) provided by (43) from GRACE (Fig. S8). To make the comparison at the drainage basin scale, we reconstructed laser altimetry-based mass changes in the observational resolution of GRACE at a lower, mascon scale by applying the resolution operator, R (Fig. S9) (38). This led to an apparent reduction in mass loss in some basins, such as NW and NE, and increased mass loss in others, such as NO and SW, by introducing similar leakage from GRACE (Fig. S10). Thus, while the R-applied laser altimetry-based reconstructions are appropriate for comparison with GRACE-based estimates, they do not represent accurate mass changes at the drainage basin scale. Notably, the RMSE between the 2003-2020 altimetry-based and GRACE reconstructions was reduced by 67% in NO and 42% in NE when the GICs were removed from the GRACE solution.

Overall, GRACE and our laser altimetry-based estimations show good agreement (Fig. 4B). The GRACE reconstruction shows a total ice mass loss of 4102 Gt (241 Gt/year) between 2003 and 2020. This falls within the range of our three reconstructions (Fig. 4B), which span from 3580 Gt (211 Gt/year) to 4164 Gt (245 Gt/year). This relationship also holds for most of the drainage basins, except the NW and NE (Fig. 4B). In the NW, GRACE shows a cumulative mass loss of 1016 Gt (60 Gt/year), exceeding the altimetry-based reconstructions ranging from 762 Gt (45 Gt/year) to 940 Gt (55 Gt/year). In the NE, GRACE reveals a total mass loss of 196 Gt (12 Gt/year), also exceeding laser altimetry-based reconstructions ranging from mass gain of 8 Gt (0.5 Gt/year) to mass loss of 76 Gt (4.5 Gt/year) (Fig. 4B). Nevertheless, we found a high similarity between the sub-decadal mass change variability of the GRACE and laser altimetry-based estimations at both the drainage basin and ice sheet scales (Fig. 4B).

Partitioning mass change into surface and dynamic components

Surface mass balance (SMB) anomaly and dynamic mass change are the two major components of the Greenland ice sheet mass change. The surface mass balance, defined as the net mass change at the ice sheet surface, equals the accumulation from precipitation minus the ablation from meltwater runoff and other processes, such as sublimation and evaporation. SMB anomaly is calculated relative to the baseline SMB of the reference period, during which total SMB is approximately equivalent to total ice discharge, such that the ice sheet is presumed to be in near equilibrium (44). Therefore, the SMB anomaly is assumed to represent the surface mass change contribution to the ice sheet mass change at the time of the anomaly. Similarly, dynamic mass change is assumed to represent the mass change incurred from the perturbations to ice flow due to ice-ocean-atmosphere interactions (2, 45, 46).

By averaging the three SMB anomaly datasets and dividing into 5-year averages, we found peak surface mass loss between 2005 and 2010 (Table S2) with significant mass loss in the ablation zone and increased mass loss in the interior of the ice sheet (Fig. 2). This could be due to a combination of enhanced surface runoff and reduced accumulation. After 2015, surface mass loss reduced and turned into mass gain in CE and SE (Fig. 2). Despite the overall slowdown of surface mass loss after 2015, the annual rates suggest another near-record mass loss in 2019 (Fig. 3). This 2019 event is more pronounced than the record melting year of 2012 in basins mostly located in northern Greenland, with 79% more surface mass loss than 2012 in CW, 56% in NW, 28% in NO, and 108% in NE (Fig. 3) (51, 52). This finding is consistent with GRACE, which observed record summer mass loss in northern Greenland, and with satellite observations of extensive surface melt in these basins in summer 2019 (47). Regionally, SW shows the highest increase in surface mass loss over a five-year scale, and it alone accounts for almost half of the total surface mass loss between 2015 and 2020 (Table S2). Furthermore, the increase in surface mass loss from 2003–2009 to 2014–2020 in the SW, as well as CW, was not restricted to the ablation zone but extended up to the ice divide (Fig. S7) due to the high melt years of 2016 and 2019 (Fig. S6). In CW, NW, and NO, surface mass loss has been increasing since the 1990s and peaked between 2010 and 2015 (Table S2). Notably, NO has become the second largest surface mass loss basin following SW between 2015 and 2020 and over the whole period (Table S2). The three drainage-basin scale SMB anomaly estimates show the largest difference in SE with a standard deviation of 13 Gt/year, much larger than the average SE surface mass loss rate of 3 Gt/year for 1994–2020 (Fig. 3). This highlights the uncertainty in SMB modeling as reported in detail in (48, 49).

Unlike the SMB anomaly that varies significantly from year to year, the dynamic mass loss of the Greenland ice sheet has been gradually increasing since the 1990s, with two maxima in 2004 and 2012 (Fig. 3). These peaks reflect the different timing of increasing dynamic mass loss in different drainage basins. For example, the 2012 peak was mainly from CW and NW. After 2013, dynamic mass loss decreased in CW. It also stabilized in NW after 2012 and started to decrease after ~2018 (Fig. 3). On the east coast in CE and SE, however, dynamic mass loss temporally reduced after the increase in the early 2000s. After that, it started to increase again and peaked in 2017 in CE and in 2019 in SE. Among all basins, SE and NW have the highest dynamic mass loss rate between 1994 and 2020 at 42 ± 14 Gt/year and 40 ± 11 Gt/year, respectively (Table S2). In contrast, insignificant dynamic mass changes are found in NO, NE, and SW compared with relatively large uncertainty from results using different firn height change datasets (Fig. 3). Nevertheless, glaciers such as Humboldt Gletscher and Zachariae Isstrom (Zachariae Isstrøm) have exhibited increased dynamic thinning (HG and ZI (6) in Fig. 1D and Fig. 2).

In this study, the dynamic mass change is calculated by subtracting solid-earth deformation and firn height change from the surface elevation change. As a result, any uncertainty in firn height change, including both SMB anomaly and firn air content change, is propagated into the dynamic mass change (Fig. 1H). Our three reconstructions with different firn height change and SMB anomaly datasets reveal high uncertainty in partitioning the total mass change into surface and dynamic components (Fig. 5, figs. S11 and S12). The IMAU-FDM, forced by RACMO2.3p2, attributes 41% of the total mass loss of the entire ice sheet between 1994 and 2020 to ice dynamics (Fig. 5), which is close to previous studies suggesting a roughly equal partitioning between surface and dynamic mass loss (10, 17). However, a much higher proportion of dynamic mass loss is derived from using the other two models: 80% with GSFC-FDM (MERRA-2 forced) and 70% with GEMB (ERA5 forced).

At the drainage basin scale, we found both similarities and differences in the partitioning results in our three reconstructions (Fig. 5). On average between 1994 and 2020, all three reconstructions show net surface mass loss in every drainage basin except SE. In SE, GSFC-FDM and GEMB indicate a net surface mass gain, while IMAU-FDM shows a considerable surface mass loss. Except in NE and SW, all three reconstructions have consistent signs of dynamic mass change. Specifically, dynamic mass loss in CE, SE, CW, and NW, and a small dynamic mass gain in NO. All three agree that dynamic mass loss exceeds surface mass loss in CE, SE, and NW. We found that the partitioning results from GSFC-FDM and GEMB are highly similar. However, in NW, using the GSFC-FDM assigns all the mass loss to ice dynamics, whereas the other two FDMs attribute only ~67% of the mass loss to ice dynamics. Using the IMAU-FDM results in greater surface mass loss than the other two in southern Greenland, especially in SE and SW. Consequently, a net dynamic mass gain is derived in SW using the IMAU-FDM, and much less mass loss is assigned to ice dynamics at the ice sheet scale. Although using different FDMs yields different absolute surface and dynamic mass loss estimates, the percentage of dynamic loss follows a consistent trend reaching a minimum around 2005–2010 before gradually increasing (Fig. 5).

The different partitioning of the three reconstructions reflects uncertainties in SMB and firn air content change modeling, and in the definition of the reference period, which presupposes the steady state of the ice sheet. Different models assume different reference periods: the IMAU-FDM uses 1960–1979, the GSFC-FDM uses 1980–1995, and GEMB uses 1979–1988. Previous studies found a high sensitivity of firn air content trend to the selection of the reference period (37, 50). Meanwhile, when calculating SMB anomalies by assuming a common reference period of 1980–1990, differences in SMB anomalies are slightly reduced in a complex manner (Fig. S13). Significant differences in SMB anomalies persist in most drainage basins (Fig. S13).

Dynamic mass change reveals complex tidewater glacier behavior

Overall, dynamic mass change is the greatest near the terminus of tidewater glaciers (Fig. 1D). It can be initiated by several processes. For example, the increased frontal ablation at the ice-ocean boundary, either due to calving or undercutting, can initiate acceleration of ice flow and dynamic thinning (45, 51). However, this relationship is modulated by many other factors, such as glacier, bed, and fjord geometry (52). To further understand how ice dynamics contributed to mass change, we examined well-sampled dynamic ice thickness change time series on selected tidewater glaciers that calve in deep fjords with warm water (53). They show the diverse patterns of dynamic ice thickness change, which is the primary component of surface elevation change near the terminus of these tidewater glaciers. The selected time series are located as close to the glacier terminus and the deep glacial trough as possible. By fusing surface elevation data since the 1970s–80s, our reconstructions provide a more complete, decadal-scale view of individual tidewater glacier dynamics than the previous study by (11).

The three well-studied large tidewater glaciers, Jakobshavn Isbrae (Sermeq Kujalleq), Kangerlussuaq (Kangerlussuaq Gletsjer), and Helheim Gletscher (Helheim Gletsjer), all retreated, accelerated, and dynamically thinned significantly in the last few decades, but with heterogeneous temporal patterns (Fig. 6). Jakobshavn Isbrae, which dominates the mass change in CW (17, 51, 54), started to show rapid dynamic thinning in the late 1990s due to ocean warming (55). Thinning continued with the weakening and disintegration of the floating ice tongue in the early 2000s (56). Starting in the late 2000s, the glacier experienced more frequent short-term variation of dynamic ice thickness change (Fig. 6). For example, it thickened by over 50 m from 2016 to 2019 near the terminus, which is likely related to ocean cooling and the existence of rigid ice mélange that restrained frontal ablation (57, 58). The 2012 and 2019 initiations of the rapid thinning are coincident with the high melt years, suggesting the potential impact of atmospheric forcing. Time series with different distances to the glacier terminus indicate propagation of these major dynamic thinning and thickening signals far inland (Fig. S14). However, the short-term, smaller-scale variations, such as the seasonal dynamic changes in 2014, are detectable only near the glacier terminus (Fig. S14). Kangerlussuaq in CE had multiple periods of thinning and stabilization since the 1980s (Fig. 6) (59), showing a pattern similar to the variations of the terminus position (Fig. S15). However, despite the similar retreat distance in the early 2000s and after 2016, dynamic thinning increased much more dramatically in the early 2000s. Helheim Gletscher had two major periods of thickening and thinning (Fig. 6) (60). Its rapid thinning in the early 2000s was followed by a short period of thickening after 2006. Thinning gradually started again in the 2010s and doesn't show the large seasonal fluctuations as in the terminus position and velocity (Fig. S16). The thinning rate decreased after 2020 (Fig. 6). Other than the climatic forcing, the complicated bedrock topography with a ridge in the middle of the fjord might have contributed to the complex behaviors of Helheim Gletscher (Fig. S16) (61).

When looking at these three large tidewater glaciers on a centennial timescale, multiple decadal thinning episodes were found in Jakobshavn Isbrae and Kangerlussuaq after 1880 (62), with the latest presented in detail in our study. These two glaciers have lost over 1000 Gt of ice since 1880 (62). Currently, dynamic mass loss from Jakobshavn Isbrae has been temporarily reduced after 2012 as the terminus reached a lateral pinning point of the fjord (Fig. 6, Fig. S15). However, the bed is over-deepening upstream and exceeds 1000 m in depth, making it at risk of further rapid retreat and dynamic mass loss if the mechanism of stabilizing the glacier is ephemeral (63). Similarly, the terminus of Kangerlussuaq is currently on a retrograde deep bed. The high variability of its terminus position and dynamic ice thickness change suggests a high sensitivity to changes in external climatic forcing. Helheim, on the other hand, hasn't been losing much mass on the centennial time scale (62). However, the dynamic ice thickness change time series near the terminus clearly shows that thinning outpaced thickening since the 1980s (Fig. 6). Thus, further investigations are needed to determine whether this glacier has transitioned to a different unsTable State (64).

Beyond these three major tidewater glaciers, numerous slower-moving glaciers also exhibited significant dynamic thinning, many with considerable temporal variations (Fig. 1D, middle maps in Fig. 3 and Fig. 5). For instance, in NW, Dietrichson and Kakivfaat Sermiat experienced slow dynamic thinning until around 2010, followed by rapid retreat, acceleration, and thinning in the early 2010s (Fig 6 and Fig. S15). Dietrichson reached a new equilibrium in the late 2010s, but Kakivfaat Sermiat began accelerating and thinning again after 2020. Steenstrup, whose calving front width is about three times larger than that of its northern neighbor (Fig. S15), Dietrichson, experienced a more gradual thinning, retreat, and acceleration. Further north, Docker Smith Gletscher W shows a long-term thinning with acceleration periods in ~2004 and 2012, followed by stabilization after ~2020 (Fig. 6). Together, patterns from the individual tidewater glaciers are reflected in the high and increasing dynamic mass loss of NW and its stabilization in the late 2010s (NW in Fig. 3). In eastern Greenland, Ikertivaq NN, located south of Helheim Gletscher, shows two cycles of rapid thinning and stabilization (Fig. 6). Tingmiarmiut Fjord, located further south, also had two thinning cycles connected by a very short thickening period (Fig. 6). Such behaviors contributed to the high dynamic mass loss rate of SE and the multiple peaks in 2005, 2010, and 2019 (SE in Fig. 3). Despite the overall small dynamic mass change signal in NO and NE, some glaciers exhibit significant dynamic thinning. Zachariae Isstrom, which is one of the outlets of the Northeast Greenland Ice Stream, dominated dynamic mass loss in NE (middle map in Fig. 5). Its dynamic thinning started to accelerate in the early 2000s (Fig. 6), coinciding with the disintegration of its floating ice shelf (65). As the glacier retreated, the calving front reconfigured into a single face in ~2012 after the northern branch was detached from the main ice stream (Fig.

S16). Since then, the terminus has retreated steadily, and the dynamic thinning and ice flow acceleration have continued (Fig. S16).

Discussion

The Greenland Ice Sheet has experienced dramatic mass loss since the 1990s, with contributions from both surface and dynamic mass loss. Regionally, NW and SE have the highest mass loss rates, mainly due to the high dynamic mass loss from tidewater glaciers (Fig. 3). Surface mass loss increased dramatically in SW, with ~14% of the SW area thinned more than 10 m between 1994 and 2020. Although NO and NE are still losing ice at a much lower rate, surface mass loss has been increasing as the ablation zone expands (34), and large tidewater glaciers have begun to show accelerated dynamic thinning (4). These changes indicate the ice sheet's vulnerability to both the atmospheric and oceanic forcing.

Our mass change reconstructions show good agreement with GRACE even during years of limited laser altimetry data availability, such as between the ICESat and ICESat-2 missions. This proves the robustness of our reconstruction methods. Meanwhile, the comparison with GRACE reveals uncertainties from both approaches. In the NE and NW, our reconstructions show lower mass loss than GRACE does. (66) found that global GIA models such as ICE_6G-D, which is used in the GRACE mascon solution, may overestimate the uplift in NE. This will lead to an overestimation of ice mass loss by GRACE. Estimation of the firn air content change alone can also lead to significantly different trends of mass changes in NE (Fig. 4). Specifically, the IMAU-FDM tends to attribute more thickening to an increase in firn air content instead of mass gain in the dry snow area of NE, resulting in a higher mass loss rate than the other two models (Fig. S17). Our reconstruction also ignores basal melt. While the basal melt estimate of 21.4 +4.4/−4.0 Gt/year from (67) indicates that it is a much smaller term than other mass change processes at the ice sheet scale, in basins like NE where the mass loss is only a few gigatons per year (Fig. 3), the estimated regional basal melt rate of 2.8 Gt/year is a substantial portion of the mass loss (67). In NW, the GIA estimate also has a significant uncertainty due to the limited availability of relative sea-level observations (68) and poorly constrained deglaciation since the Little Ice Age in most GIA models, such as ICE_6G-D used by the GSFC GRACE solution (31, 69). Uneven spatiotemporal sampling of laser altimetry, such as rapidly thinning tidewater glaciers that were not surveyed by airborne missions, and the lack of SERAC elevation change time series near tidewater glacier termini due to the sparse coverage of ICESat groundtracks (Fig. S1), could also introduce additional uncertainty to our altimetry-based reconstructions. Overall, our reconstruction, together with GRACE observations, demonstrates both the reliability and uncertainty of drainage-basin-scale mass change estimates. These results provide critical information for evaluating and calibrating ice-sheet models using drainage basin mass change.

Using three different firn height change datasets, we observed a high uncertainty in the partitioning of surface and dynamic mass loss. In our reconstruction, different estimates of the firn height change trend led to different partitioning results. However, previous partitioning estimates also depended directly on the modeled SMB and the assumed reference period. For example, in IMBIE2, the SMB anomaly is derived by averaging the SMB from three regional climate models (RACMO2.3p2, MARv3.6, and HIRHAM) and removing the mean SMB between 1980 and 1990, the assumed reference period (10). Despite being unable to determine the exact ratios, our results improve the understanding of partitioning by evaluating its uncertainty at the ice sheet and drainage basin scale, as well as the spatiotemporal variability of surface and dynamic mass change. Further investigations are needed to understand the relative contributions of surface and dynamic processes to ice sheet mass loss.

Taking advantage of the small footprint size of laser altimetry, our reconstruction produced a robust estimate of the decadal trend and interannual variability of dynamic ice thickness change near the terminus of many tidewater glaciers. These new results confirmed the complex spatiotemporal variability of outlet glacier behavior (11) and provided insight into the timing and evolution of ice-dynamics events over an extended period from the 1970s–80s to 2022. These dynamic ice thickness change observations, together with other observations such as terminus position and surface ice flow velocity, depict a more comprehensive picture of the dynamic behaviors of individual tidewater glaciers. This is critical for identifying the processes driving the changes of individual tidewater glaciers. For example, the potential impact of local factors on the asynchronous start of rapid thinning and retreating of tidewater glaciers in the NW and CW. We need to continue monitoring tidewater glaciers because of the potential for rapid reconfiguration of the ice sheet margin (70) and the risk of further rapid retreat and dynamic mass loss following the substantial surface lowering driven by dynamic thinning and surface ablation in recent decades (64). We also detected dynamic ice thickness change signals in the interior of the ice sheet, such as the widespread dynamic thickening in the interior of NO, NE, and SW (Fig. S11). However, it remains unclear whether the dynamic thickening reflects errors in firn height change datasets (66, 71), a slowdown of the ice flow, such as in the land-terminating margins of SW (72), or the ice sheet still responding to long-term changes in ice rheology (73). Dynamic changes are also observed far upstream of many glaciers' termini (74–76). These results highlight the importance of improving our observations and understanding of ice dynamics not only near the ice sheet margin but also in the ice sheet interior.

Materials and Methods

Over 54,000 surface elevation change time series were reconstructed using the Surface Elevation Reconstruction And Change detection (SERAC) framework across the Greenland Ice Sheet, which combines airborne and satellite laser altimetry (11, 27, 59). These elevation change time series were corrected for solid Earth deformation and firn height changes to isolate dynamic ice thickness variations. To explicitly quantify the substantial uncertainty associated with firn air content, firn height changes were estimated using an ensemble of three independent firn densification models: IMAU-FDM v1.2G forced by RACMO2.3p2 (33, 34), GSFC-FDM v1.2.1 forced by MERRA-2 (35, 36), and GEMB v1.0 forced by corrected ERA5 (37). The residual dynamic thickness change was temporally interpolated using localized spline methods, and subsequently spatially interpolated to a 1-km grid using ordinary kriging. It's then combined with surface mass balance anomalies to estimate total mass change, with the modeled elastic response of the solid Earth removed. These reconstructed mass changes were compared with the NASA GSFC GRACE mascon solution utilizing a novel comparison framework specifically designed to ensure spatial consistency and to explicitly account for peripheral glaciers and ice caps (15, 38). Please see SI Text for details of the methods.

Acknowledgments

B.M.C., A.F.S., S.N., K.P., H.G., and I.P. acknowledge support by National Aeronautics and Space Administration grant 80NSSC21K0915. S.N., M.J.C., B.M.C., D.F., B.L., A.F.S., and H.G. acknowledge support from National Aeronautics and Space Administration grant 80NSSC21K0322. S.A. acknowledges support from NASA grants 23-SLCST23-0008, 23-MAP23-0017, and 21-ESI21-0011. A part of this study was conducted at the Jet Propulsion Laboratory, California Institute of Technology, under a contract with the National Aeronautics and Space Administration. M.B. acknowledges OCEAN ICE, which is funded by the European Union, Horizon Europe Funding Programme for research and innovation under grant agreement Nr. 101060452 and the UK Research and Innovation (UKRI) under the UK government's Horizon Europe funding Guarantee 10044471. M.R.v.d.B. acknowledges support from the Netherlands Organisation for Scientific Research (NWO) summit grant SUMMIT 1.034 EMBRACER. D.F.acknowledges support from the NASA Sea-Level Change Team (DF). D.F. and B.M.

acknowledge support from the NASA ICESat-2 Project Science Office. B.N. acknowledges support from The Fonds de la Recherche Scientifique de Belgique – F.R.S.-FNRS.

References

1. T. Frederikse, *et al.*, The causes of sea-level rise since 1900. *Nature* **584**, 393–397 (2020).

2. H. Goelzer, *et al.*, The future sea-level contribution of the Greenland ice sheet: a multi-model ensemble study of ISMIP6. *The Cryosphere* **14**, 3071–3096 (2020).

3. M. R. van den Broeke, *et al.*, On the recent contribution of the Greenland ice sheet to sea level change. *The Cryosphere* **10**, 1933–1946 (2016).

4. E. A. Hill, J. R. Carr, C. R. Stokes, G. H. Gudmundsson, Dynamic changes in outlet glaciers in northern Greenland from 1948 to 2015. *The Cryosphere* **12**, 3243–3263 (2018).

5. L. Montgomery, L. Koenig, J. T. M. Lenaerts, P. K. Munneke, Accumulation rates (2009–2017) in Southeast Greenland derived from airborne snow radar and comparison with regional climate models. *Ann. Glaciol.* **61**, 225–233 (2020).

6. G. A. Catania, L. A. Stearns, T. A. Moon, E. M. Enderlin, R. H. Jackson, Future Evolution of Greenland's Marine-Terminating Outlet Glaciers. *J. Geophys. Res.-Earth Surf.* **125**, e2018JF004873 (2020).

7. N. Jullien, A. J. Tedstone, H. Machguth, N. B. Karlsson, V. Helm, Greenland Ice Sheet Ice Slab Expansion and Thickening. *Geophys. Res. Lett.* **50**, e2022GL100911 (2023).

8. Y. Choi, H. Seroussi, M. Morlighem, N.-J. Schlegel, A. Gardner, Impact of time-dependent data assimilation on ice flow model initialization and projections: a case study of Kjer Glacier, Greenland. *The Cryosphere* **17**, 5499–5517 (2023).

9. D. Felikson, *et al.*, Progress and future directions in constraining uncertainties in sea-level projections using observations. *Nat. Clim. Change* **15**, 1039–1051 (2025).

10. A. Shepherd, *et al.*, Mass balance of the Greenland Ice Sheet from 1992 to 2018. *Nature* **579**, 233–239 (2020).

11. B. M. Csatho, *et al.*, Laser altimetry reveals complex pattern of Greenland Ice Sheet dynamics. *Proc. Natl. Acad. Sci. U. S. A.* **111**, 18478–18483 (2014).

12. J. Nilsson, A. S. Gardner, Elevation Change of the Greenland Ice Sheet and its Peripheral Glaciers: 1992-2023. *Earth Syst. Sci. Data Discuss.* 1–28 (2024). https://doi.org/10.5194/essd-2024-311.

13. B. D. Tapley, *et al.*, Contributions of GRACE to understanding climate change. *Nat. Clim. Change* **9**, 358–369 (2019).

14. B. D. Tapley, S. Bettadpur, J. C. Ries, P. F. Thompson, M. M. Watkins, GRACE Measurements of Mass Variability in the Earth System. *Science* **305**, 503–505 (2004).

15. S. B. Luthcke, *et al.*, Antarctica, Greenland and Gulf of Alaska land-ice evolution from an iterated GRACE global mascon solution. *J. Glaciol.* **59**, 613–631 (2013).

16. E. Rignot, J. E. Box, E. Burgess, E. Hanna, Mass balance of the Greenland ice sheet from 1958 to 2007. *Geophys. Res. Lett.* **35** (2008).

17. J. Mouginot, *et al.*, Forty-six years of Greenland Ice Sheet mass balance from 1972 to 2018. *Proc. Natl. Acad. Sci. U. S. A.* **116**, 9239–9244 (2019).

18. K. D. Mankoff, *et al.*, Greenland ice sheet mass balance from 1840 through next week. *Earth Syst. Sci. Data* **13**, 5001–5025 (2021).

19. I. N. Otosaka, *et al.*, Mass balance of the Greenland and Antarctic ice sheets from 1992 to 2020. *Earth Syst. Sci. Data* **15**, 1597–1616 (2023).

20. J. A. MacGregor, *et al.*, The Scientific Legacy of NASA's Operation IceBridge. *Rev. Geophys.* **59**, e2020RG000712 (2021).

21. H. J. Zwally, *et al.*, ICESat's laser measurements of polar ice, atmosphere, ocean, and land. *J. Geodyn.* **34**, 405–445 (2002).

22. T. Markus, *et al.*, The Ice, Cloud, and land Elevation Satellite-2 (ICESat-2): Science requirements, concept, and implementation. *Remote Sens. Environ.* **190**, 260–273 (2017).

23. H. D. Pritchard, R. J. Arthern, D. G. Vaughan, L. A. Edwards, Extensive dynamic thinning on the margins of the Greenland and Antarctic ice sheets. *Nature* **461**, 971–975 (2009).

24. B. Smith, *et al.*, Pervasive ice sheet mass loss reflects competing ocean and atmosphere processes. *Science* **368**, 1239-+ (2020).

25. J. Nilsson, A. S. Gardner, F. S. Paolo, Elevation change of the Antarctic Ice Sheet: 1985 to 2020. *Earth Syst. Sci. Data* **14**, 3573–3598 (2022).

26. S. A. Khan, *et al.*, Smoothed monthly Greenland ice sheet elevation changes during 2003–2023. *Earth Syst. Sci. Data* **17**, 3047–3071 (2025).

27. T. Schenk, B. Csatho, A New Methodology for Detecting Ice Sheet Surface Elevation Changes From Laser Altimetry Data. *Ieee Trans. Geosci. Remote Sens.* **50**, 3302–3316 (2012).

28. N. J. Korsgaard, *et al.*, Digital elevation model and orthophotographs of Greenland based on aerial photographs from 1978-1987. *Sci. Data* **3**, 160032 (2016).

29. S. A. Khan, *et al.*, Greenland Mass Trends From Airborne and Satellite Altimetry During 2011–2020. *J. Geophys. Res. Earth Surf.* **127**, e2021JF006505 (2022).

30. M. McMillan, *et al.*, A high-resolution record of Greenland mass balance. *Geophys. Res. Lett.* **43**, 7002–7010 (2016).

31. S. Adhikari, *et al.*, Decadal to Centennial Timescale Mantle Viscosity Inferred From Modern Crustal Uplift Rates in Greenland. *Geophys. Res. Lett.* **48**, e2021GL094040 (2021).

32. G. A. Milne, *et al.*, The influence of lateral Earth structure on glacial isostatic adjustment in Greenland. *Geophys. J. Int.* **214**, 1252–1266 (2018).

33. M. Brils, P. Kuipers Munneke, W. J. van de Berg, M. van den Broeke, Improved representation of the contemporary Greenland ice sheet firn layer by IMAU-FDM v1.2G. *Geosci. Model Dev.* **15**, 7121–7138 (2022).

34. B. Noel, W. J. van de Berg, S. Lhermitte, M. R. van den Broeke, Rapid ablation zone expansion amplifies north Greenland mass loss. *Sci. Adv.* **5**, eaaw0123 (2019).

35. B. Medley, T. A. Neumann, H. J. Zwally, B. E. Smith, C. M. Stevens, Simulations of firn processes over the Greenland and Antarctic ice sheets: 1980–2021. *The Cryosphere* **16**, 3971–4011 (2022).

36. R. Gelaro, *et al.*, The Modern-Era Retrospective Analysis for Research and Applications, Version 2 (MERRA-2). *J. Clim.* **30**, 5419–5454 (2017).

37. A. S. Gardner, N.-J. Schlegel, E. Larour, Glacier Energy and Mass Balance (GEMB): a model of firn processes for cryosphere research. *Geosci. Model Dev.* **16**, 2277–2302 (2023).

38. B. D. Loomis, S. B. Luthcke, T. J. Sabaka, Regularization and error characterization of GRACE mascons. *J. Geod.* **93**, 1381–1398 (2019).

39. S. B. Simonsen, V. R. Barletta, W. T. Colgan, L. S. Sorensen, Greenland Ice Sheet Mass Balance (1992-2020) From Calibrated Radar Altimetry. *Geophys. Res. Lett.* **48**, e2020GL091216 (2021).

40. P. Rastner, *et al.*, The first complete inventory of the local glaciers and ice caps on Greenland. *The Cryosphere* **6**, 1483–1495 (2012).

41. K. K. Kjeldsen, S. A. Khan, W. T. Colgan, J. A. MacGregor, R. S. Fausto, Time-Varying Ice Sheet Mask: Implications on Ice-Sheet Mass Balance and Crustal Uplift. *J. Geophys. Res. Earth Surf.* **125**, e2020JF005775 (2020).

42. W. Richard Peltier, D. F. Argus, R. Drummond, Comment on “An Assessment of the ICE-6G_C (VM5a) Glacial Isostatic Adjustment Model” by Purcell et al. *J. Geophys. Res. Solid Earth* **123**, 2019–2028 (2018).

43. S. A. Khan, *et al.*, Accelerating Ice Loss From Peripheral Glaciers in North Greenland. *Geophys. Res. Lett.* **49**, e2022GL098915 (2022).

44. H. A. Fricker, R. C. Warner, I. Allison, Mass balance of the Lambert Glacier–Amery Ice Shelf system, East Antarctica: a comparison of computed balance fluxes and measured fluxes. *J. Glaciol.* **46**, 561–570 (2000).

45. F. M. Nick, A. Vieli, I. M. Howat, I. Joughin, Large-scale changes in Greenland outlet glacier dynamics triggered at the terminus. *Nat. Geosci.* **2**, 110–114 (2009).

46. K. M. Cuffey, W. S. B. Paterson, *The physics of glaciers*, Fourth edition (Elsevier, 2010).

47. R. I. Cullather, *et al.*, Anomalous Circulation in July 2019 Resulting in Mass Loss on the Greenland Ice Sheet. *Geophys. Res. Lett.* **47**, e2020GL087263 (2020).

48. X. Fettweis, *et al.*, GrSMBMIP: intercomparison of the modelled 1980–2012 surface mass balance over the Greenland Ice Sheet. *The Cryosphere* **14**, 3935–3958 (2020).

49. B. Vandecrux, *et al.*, The firn meltwater Retention Model Intercomparison Project (RetMIP): evaluation of nine firn models at four weather station sites on the Greenland ice sheet. *The Cryosphere* **14**, 3785–3810 (2020).

50. P. Kuipers Munneke, *et al.*, Elevation change of the Greenland Ice Sheet due to surface mass balance and firn processes, 1960–2014. *The Cryosphere* **9**, 2009–2025 (2015).

51. M. D. King, *et al.*, Dynamic ice loss from the Greenland Ice Sheet driven by sustained glacier retreat. *Commun. Earth Environ.* **1**, 1 (2020).

52. C. Bunce, J. R. Carr, P. W. Nienow, N. Ross, R. Killick, Ice front change of marine-terminating outlet glaciers in northwest and southeast Greenland during the 21st century. *J. Glaciol.* **64**, 523–535 (2018).

53. M. Wood, *et al.*, Ocean forcing drives glacier retreat in Greenland. *Sci. Adv.* **7**, eaba7282 (2021).

54. W. Kochtitzky, *et al.*, Closing Greenland's Mass Balance: Frontal Ablation of Every Greenlandic Glacier From 2000 to 2020. *Geophys. Res. Lett.* **50**, e2023GL104095 (2023).

55. D. M. Holland, R. H. Thomas, B. de Young, M. H. Ribergaard, B. Lyberth, Acceleration of Jakobshavn Isbræ triggered by warm subsurface ocean waters. *Nat. Geosci.* **1**, 659–664 (2008).

56. I. Joughin, *et al.*, Continued evolution of Jakobshavn Isbrae following its rapid speedup. *J. Geophys. Res. Earth Surf.* **113** (2008).

57. A. Khazendar, *et al.*, Interruption of two decades of Jakobshavn Isbrae acceleration and thinning as regional ocean cools. *Nat. Geosci.* **12**, 277-+ (2019).

58. I. Joughin, D. E. Shean, B. E. Smith, D. Floricioiu, A decade of variability on Jakobshavn Isbrae: ocean temperatures pace speed through influence on melange rigidity. *Cryosphere* **14**, 211–227 (2020).

59. T. Schenk, B. Csatho, C. van der Veen, D. McCormick, Fusion of multi-sensor surface elevation data for improved characterization of rapidly changing outlet glaciers in Greenland. *Remote Sens. Environ.* **149**, 239–251 (2014).

60. L. M. Kehrl, I. Joughin, D. E. Shean, D. Floricioiu, L. Krieger, Seasonal and interannual variabilities in terminus position, glacier velocity, and surface elevation at Helheim and Kangerlussuaq Glaciers from 2008 to 2016. *J. Geophys. Res.-Earth Surf.* **122**, 1635–1652 (2017).

61. L. Ultee, D. Felikson, B. Minchew, L. A. Stearns, B. Riel, Helheim Glacier ice velocity variability responds to runoff and terminus position change at different timescales. *Nat. Commun.* **13**, 6022 (2022).

62. S. A. Khan, *et al.*, Centennial response of Greenland's three largest outlet glaciers. *Nat. Commun.* **11**, 5718 (2020).

63. C. Schoof, Ice sheet grounding line dynamics: Steady states, stability, and hysteresis. *J. Geophys. Res. Earth Surf.* **112** (2007).

64. J. J. Williams, N. Gourmelen, P. Nienow, C. Bunce, D. Slater, Helheim Glacier Poised for Dramatic Retreat. *Geophys. Res. Lett.* **48**, e2021GL094546 (2021).

65. J. Mouginot, *et al.*, Fast retreat of Zachariæ Isstrøm, northeast Greenland. *Science* **350**, 1357–1361 (2015).

66. M. T. Kappelsberger, *et al.*, Modeled and Observed Bedrock Displacements in North-East Greenland Using Refined Estimates of Present-Day Ice-Mass Changes and Densified GNSS Measurements. *J. Geophys. Res. Earth Surf.* **126**, e2020JF005860 (2021).

67. N. B. Karlsson, *et al.*, A first constraint on basal melt-water production of the Greenland ice sheet. *Nat. Commun.* **12**, 3461 (2021).

68. B. S. Lecavalier, *et al.*, A model of Greenland ice sheet deglaciation constrained by observations of relative sea level and ice extent. *Quat. Sci. Rev.* **102**, 54–84 (2014).

69. S. A. Khan, *et al.*, Geodetic measurements reveal similarities between post–Last Glacial Maximum and present-day mass loss from the Greenland ice sheet. *Sci. Adv.* **2**, e1600931 (2016).

70. T. A. Moon, A. S. Gardner, B. Csatho, I. Parmuzin, M. A. Fahnestock, Rapid Reconfiguration of the Greenland Ice Sheet Coastal Margin. *J. Geophys. Res. Earth Surf.* **125**, e2020JF005585 (2020).

71. B. E. Smith, *et al.*, Evaluating Greenland surface-mass-balance and firn-densification data using ICESat-2 altimetry. *The Cryosphere* **17**, 789–808 (2023).

72. J. J. Williams, N. Gourmelen, P. Nienow, Dynamic response of the Greenland ice sheet to recent cooling. *Sci. Rep.* **10**, 1647 (2020).

73. J. A. MacGregor, *et al.*, Holocene deceleration of the Greenland Ice Sheet. *Science* **351**, 590–593 (2016).

74. S. A. Khan, *et al.*, Extensive inland thinning and speed-up of Northeast Greenland Ice Stream. *Nature* **611**, 727–732 (2022).

75. J. J. Williams, N. Gourmelen, P. Nienow, Complex multi-decadal ice dynamical change inland of marine-terminating glaciers on the Greenland Ice Sheet. *J. Glaciol.* **67**, 833–846 (2021).

76. A. Løkkegaard, *et al.*, Ice acceleration and rotation in the Greenland Ice Sheet interior in recent decades. *Commun. Earth Environ.* **5**, 1–12 (2024).

77. B. Vandecrux, *et al.*, Firn data compilation reveals widespread decrease of firn air content in western Greenland. *The Cryosphere* **13**, 845–859 (2019).

78. P. Shekhar, B. Csatho, T. Schenk, C. Roberts, A. K. Patra, ALPS: A Unified Framework for Modeling Time Series of Land Ice Changes. *Ieee Trans. Geosci. Remote Sens.* **59**, 6466–6481 (2021).

79. I. Joughin, B. E. Smith, I. M. Howat, A complete map of Greenland ice velocity derived from satellite data collected over 20 years. *J. Glaciol.* **64**, 1–11 (2018).

Figures and Tables

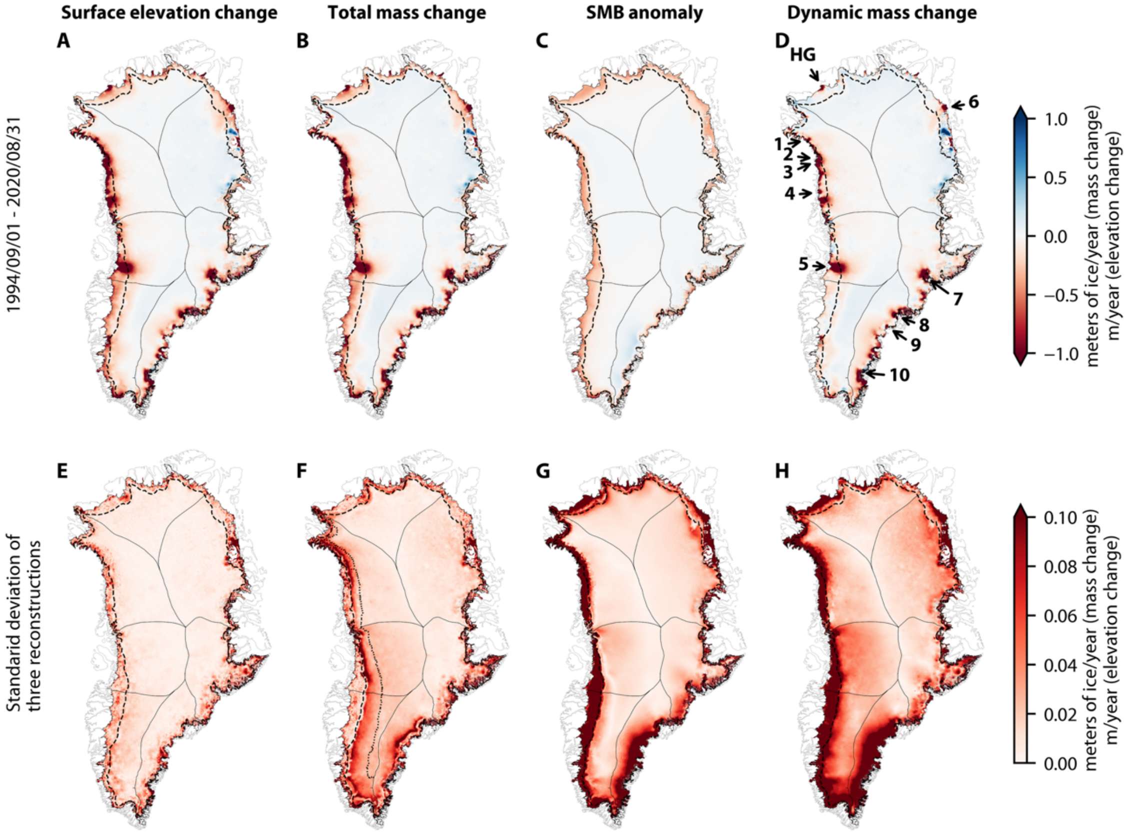

Figure 1. Mean annual surface elevation and mass change of the Greenland Ice Sheet between 1994 and 2020. (A to D) Mean annual rates of surface elevation change, total mass change, surface mass balance (SMB) anomaly, and dynamic mass change between September 1, 1994, and August 31, 2020. These are averaged over three reconstructions using laser altimetry with firn height change datasets from IMAU-FDM, GSFC-FDM, and GEMB. (E to H) The standard deviations of the three 1994–2020 reconstructions for the corresponding variables in A to D using different FDMs. Drainage basin outlines are shown as black solid lines (17). The equilibrium-line altitude (ELA) (SMB=0 for 1994–2020 from MERRA-2) is shown as a black dashed line. On F, the boundary between the percolation and dry snow zones in western Greenland from (77) is shown as a black dotted line. The locations of the glaciers in Fig. 6 and Figs. S15-16 are annotated with numbers and arrows on D: 1, Docker Smith Gletscher W; 2, Dietrichson (Dietrichson Gletsjer); 3, Steenstrup 4, Kakivfaat Sermiat (Kakiffaat Sermiat); 5, Jakobshavn Isbrae (Sermeq Kujalleq); 6, Zachariae Isstrom (Zachariae Isstrøm); 7, Kangerlussuaq (Kangerlussuaq Gletsjer); 8, Helheim Gletscher (Helheim Gletsjer); 9, Ikertivaq NN; 10, Tingmiarmiut Fjord. Humboldt Gletscher (HG) is also annotated on D.

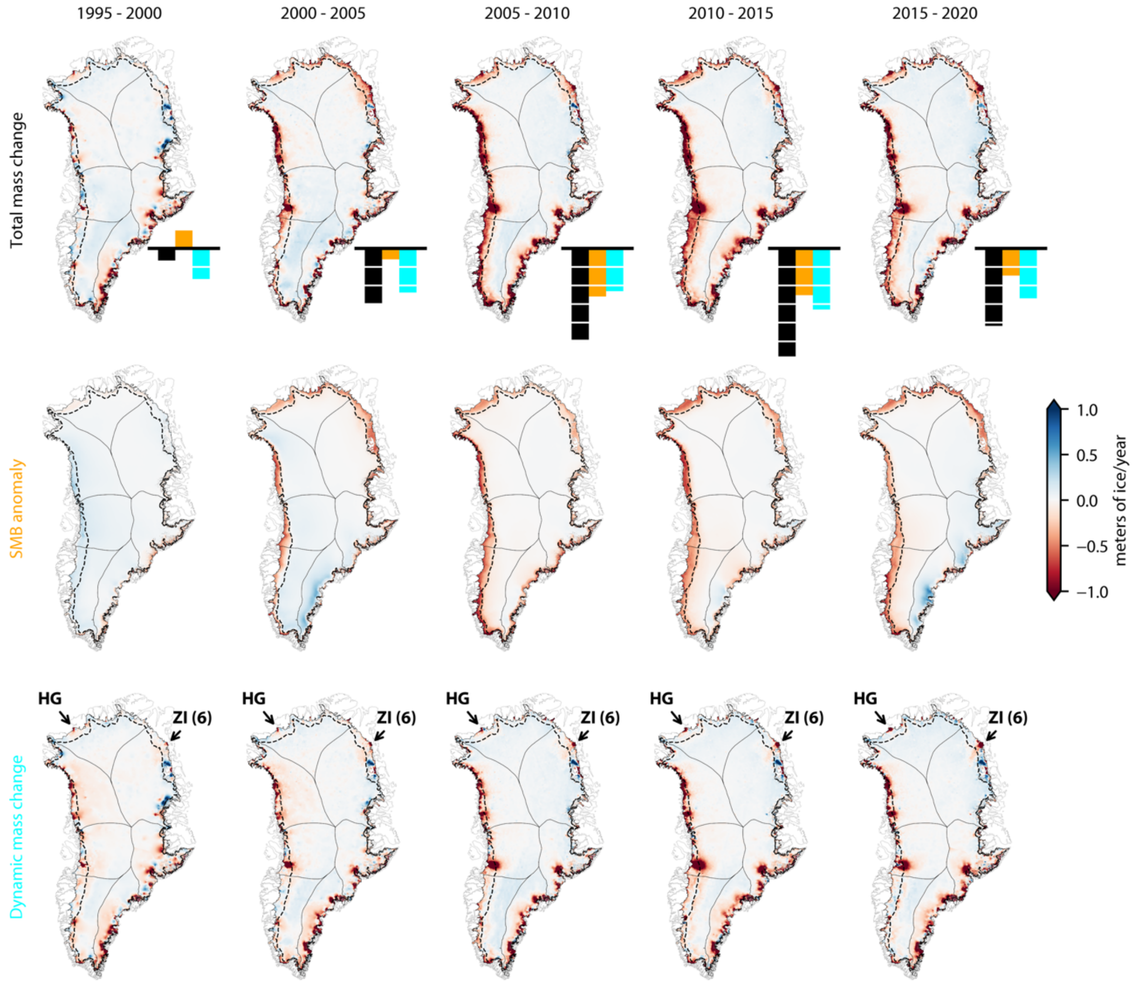

Figure 2. Maps of partitioned Greenland Ice Sheet mass changes over five-year periods. Mean annual total, surface (SMB anomaly), and dynamic mass change maps (averaged across three reconstructions using different FDMs) for each five-year period since September 1, 1995. Locations of Humboldt Gletscher (HG) and Zachariae Isstrom (ZI, glacier 6) are annotated on the dynamic mass change maps. The drainage basins' outlines and the 1994–2020 ELA are shown as black solid and dashed lines, respectively. The bar plots at the lower right of the total mass change maps show the average total mass change rate (black bars) divided into SMB anomaly (orange bars) and dynamic mass change (cyan bars) over each 5-year period. White lines mark 50 Gt/yr intervals. The thick horizontal black line is the reference 0 line, with bars above it indicating mass gain and bars below it indicating mass loss.

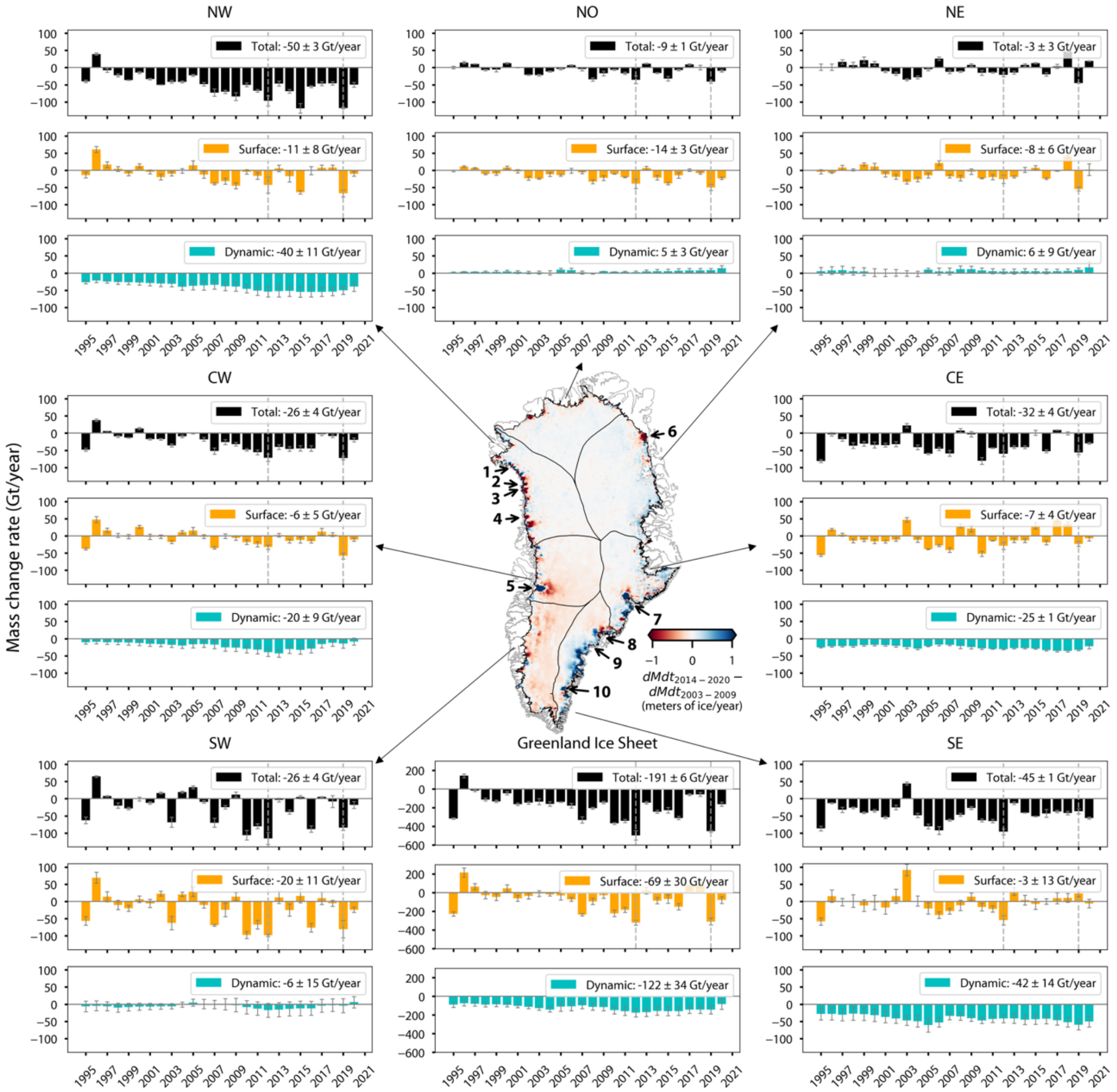

Figure 3. Annual mass change time series of Greenland Ice Sheet and drainage basins, and mass change difference between the periods 2003–2009 and 2014–2020. The panels with three bar plots show the average annual mass change of our three reconstructions in Gt/year in each drainage basin and the whole Greenland Ice Sheet. Total mass change rates are in black, surface mass balance anomaly in orange, and dynamic mass change rates in cyan. Estimates of the mean 1994–2020 annual mass change rates and their uncertainty in each region are also listed. The record melt years of 2012 and 2019 are annotated with a grey vertical dashed line in the total and surface mass change plots. The error bars represent the standard deviation of our three reconstructions using the three FDMs. The middle map shows the difference in mean annual total mass change between 2003/09/01–2009/08/31 and 2014/09/01–2020/08/31. The red color on the map indicates increased mass loss or decreased mass gain during 2014–2020 compared to 2003–2009, and vice versa. The locations of the glaciers in Fig. 6 are annotated on this map.

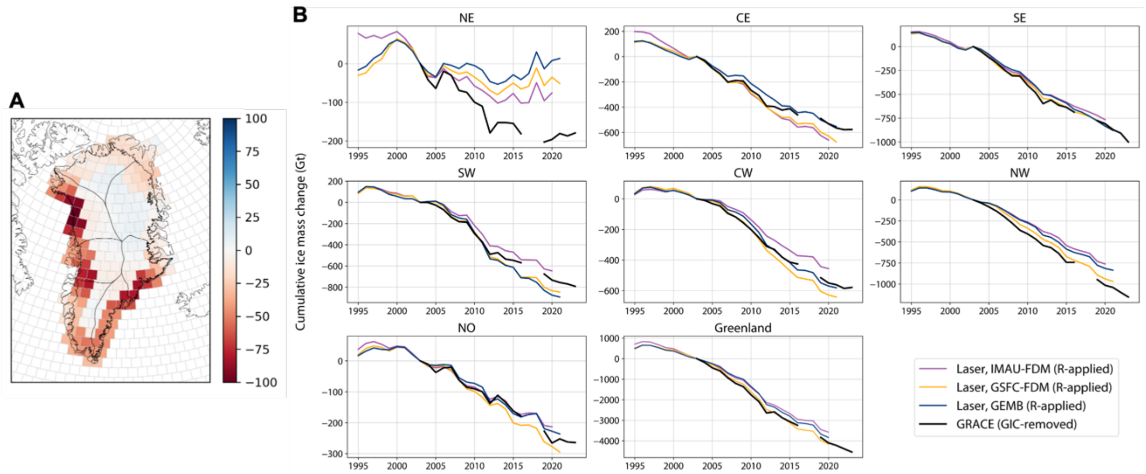

Figure 4. Comparison of mass change reconstructed using laser altimetry and GRACE. (A) Total 2003-2020 mass change from GRACE observations with mass change from peripheral glaciers and ice caps (GICs) removed. The assignments of each GRACE mascon into the drainage basins are shown in Fig. S8A. (B) Comparison of cumulative drainage-basin and Greenland Ice Sheet mass changes from laser altimetry (this study) and GRACE. The laser altimetry-based reconstructions with the GIA model replaced and the resolution operator (R) applied are shown in solid purple (IMAU-FDM), orange (GSFC-FDM), and blue (GEMB) lines (second row in Fig. S9). The solid black lines are the GIC-removed GRACE mass changes from NASA GSFC in A.

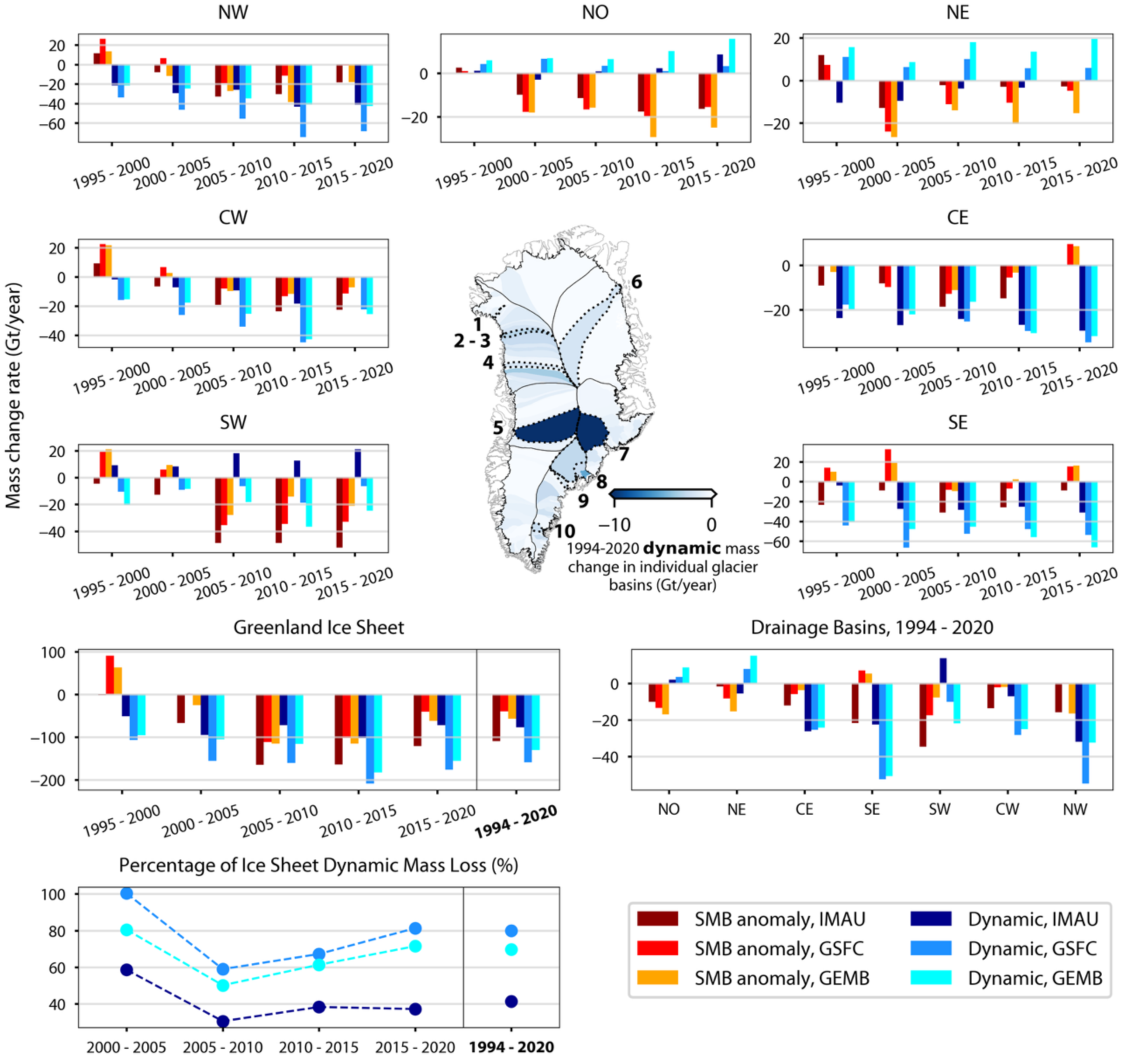

Figure 5. Five-year and 1994-2020 average surface and dynamic mass change rates from partitioned laser altimetry reconstructions. The red bars are SMB anomalies, and the blue bars are dynamic mass change rates calculated using laser altimetry with different FDMs. Drainage basin-scale partitioning from 1994 to 2020 is summarized in the panel above the legend. The percentages of dynamic mass loss relative to the total mass loss are shown as blue points in the lower left panel. The middle map shows the individual glacier basins colored by the average 1994 to 2020 dynamic mass change rates, averaged from our three reconstructions. Drainage basin and glacier basin outlines are from (17). The basins of the glaciers in Fig. 6 are highlighted using dotted black lines.

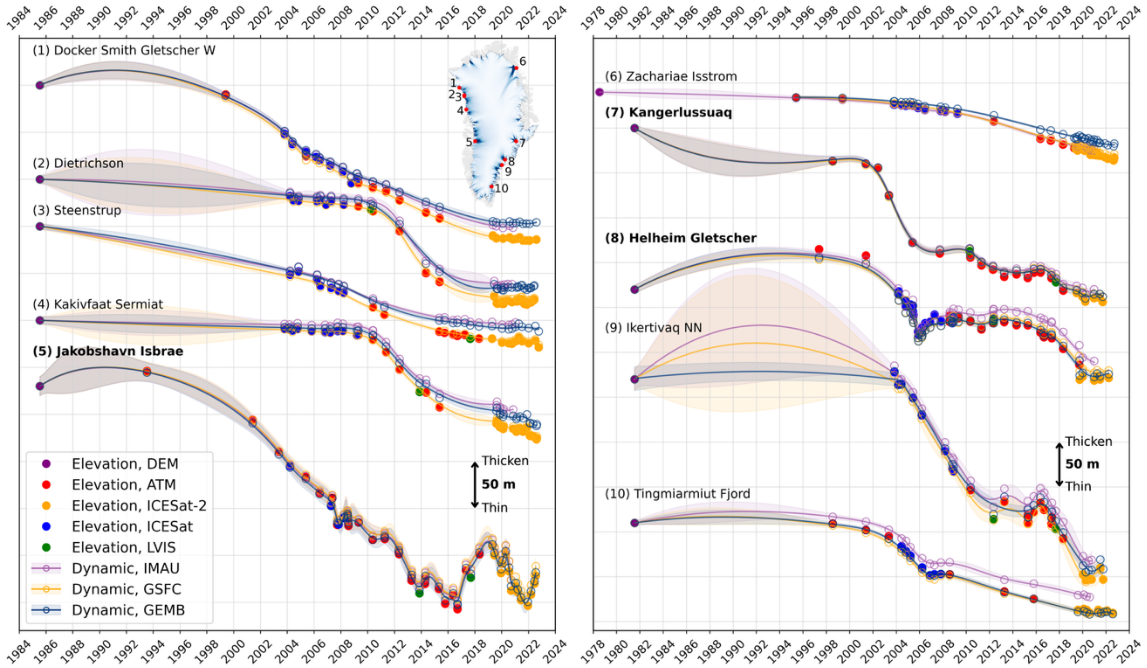

Figure 6. Elevation and dynamic ice thickness change of selected tidewater glaciers. Surface elevation changes are shown as points, colored by laser altimetry missions or sensors. Dynamic ice thickness changes derived using different firn height change datasets are shown as colored circles: purple for the IMAU-FDM, orange for the GSFC-FDM, and blue for GEMB. Lines represent interpolated dynamic ice thickness changes using the Approximation by Localized Penalized Spline (ALPS) method with 95% t-confidence intervals (colored band) (78). A downward trend in the time series indicates glacier thinning, and an upward trend indicates thickening. The 10 selected glaciers are divided into west coast (left panel) and east coast (right panel), with the three large outlet glaciers, Jakobshavn Isbrae, Kangerlussuaq, and Helheim Gletscher labeled with bold text. The inset shows the locations of the selected glaciers (red dots) on the 1995-2015 Greenland velocity mosaic from (79). Glacier elevation, dynamic ice thickness, ice velocity, and terminus position change time series, with time-series locations on bed-elevation maps, are in Figs. S15 and S16. Exact locations and further information about these time series are listed in Table S3.

Table 1. Mass change rates of the Greenland Ice Sheet and its constituent drainage basins. Mean annual total mass change rates every five years since 1995, as well as from 1994 to 2020, from the September 1 of the start year to the August 31 of the end year. These rates are averaged from our three reconstructions with different FDMs and rounded to integers. The uncertainty represents the standard deviation of the three reconstructions. Five-year average surface and dynamic mass change rates are presented in Table S2.

Region	**Mean mass change rate (Gt/year)**					
	1995–2000	**2000–2005**	**2005–2010**	**2010–2015**	**2015–2020**	**1994–2020**
Greenland	-34 ± 15	-149 ± 13	-246 ± 18	-291 ± 19	-209 ± 11	-191 ± 6
NE	12 ± 7	-19 ± 2	-1 ± 4	-6 ± 1	1 ± 3	-3 ± 3
CE	-24 ± 6	-29 ± 5	-36 ± 6	-37 ± 3	-26 ± 2	-32 ± 4
SE	-29 ± 1	-33 ± 3	-58 ± 3	-53 ± 2	-43 ± 5	-45 ± 1
SW	5 ± 3	-2 ± 2	-40 ± 7	-47 ± 8	-39 ± 6	-26 ± 4
CW	7 ± 1	-16 ± 2	-35 ± 6	-52 ± 7	-30 ± 5	-26 ± 4
NW	-8 ± 1	-38 ± 1	-65 ± 7	-80 ± 5	-63 ± 4	-50 ± 3
NO	5 ± 1	-12 ± 1	-11 ± 2	-18 ± 2	-10 ± 2	-9 ± 1

PNAS

Supporting Information for
Nearly three decades of laser altimetry reveal strong regional contrasts and glacier-driven ice losses in Greenland

Hui Gao, Beata M Csatho, Anton F Schenk, Michael J Croteau, Surendra Adhikari, Ivan Parmuzin, Nicole-Jeanne Schlegel, Max Brils, Michiel R. van den Broeke, Denis Felikson, Bryant Loomis, Brooke Medley, Brice Noël, Sophie Nowicki, and Kristin Poinar

Hui Gao
Email: hgao7@buffalo.edu

This PDF file includes:

Supporting text
Figures S1 to S17
Tables S1 to S3
Legends for Datasets S1 to S3
SI References

Other supporting materials for this manuscript include the following:

Datasets S1 to S3

Supporting Information Text

Reconstruction of Greenland Ice Sheet Mass Change

Surface elevation changes time series. Surface elevation change time series are reconstructed using the SERAC method (Surface Elevation Reconstruction And Change detection) (1–3). We used SERAC to fuse airborne and satellite laser altimetry surface elevation measurements from NASA's Program for Regional Climate Assessment and Operation IceBridge missions (Airborne Topographic Mapping system (ATM) and Land, Vegetation, and Ice Sensor (LVIS)), ICESat, and ICESat-2 satellite altimetry between 1993 and 2022 (Fig. S1) (4–6), and included DEMs from stereo aerial photographs between 1978 and 1987 near the ice sheet margin (7). Because the DEMs cover only the ice sheet margin, we use them to contextualize the altimetry-based reconstruction for 1993-2022, but do not extend the ice sheet mass change estimation back to the 1980s. SERAC estimates time series of surface elevation change and absolute elevations at the centroids of all altimetry observations within ~1km2 surface patches by modeling its shape with a third-order polynomial fit. It assumes that the shape of each surface patch is time-invariant. The locations of the time series are primarily determined by ICESat ground-track crossovers and ICESat's overlaps with ATM or LVIS (8) to obtain longer time series and correct for surface shape at the same time. The SERAC time series dataset was thinned by imposing a minimum distance of 500 m between time series locations and selecting the longest time series, i.e., those consisting of the most time observational periods (epochs). We obtained over 54,000 time series across the Greenland Ice Sheet with irregular temporal spacing and various lengths (Fig. S2A). We removed time series with high uncertainties based on the quality of the SERAC's least-squares solution. We identified epochs when the ice sheet boundary retreated behind the time series locations on floating ice by comparing absolute ice surface elevations with ocean surface elevation estimated by the GGEOID16 geoid height (9). We flagged and further discarded data points within 10 m elevation above the open ocean water and didn't use them. Finally, outliers within each time series were detected using a multi-step statistical approach. These outliers were flagged and excluded from this reconstruction.

Solid Earth Corrections. To convert surface elevation change to ice thickness change, we first correct for the solid Earth's viscoelastic response to the long-term surface mass redistribution. We use glacial isostatic adjustment (GIA) uplift rates that combine estimations from (10) and (11). The GIA model from (10) accounts for the 3-D Earth structure using multiple realizations of mantle viscosity and lithosphere thickness and considers North Hemispheric deglaciation since the Last Glacial Maximum with improved loading history in Greenland based on the Huy3 reconstruction (12). (11) modeled ongoing viscoelastic solid Earth response to post-Little Ice Age (LIA) deglaciation – a signal vastly overlooked by typical GIA models – using large ensembles that vary lithosphere thickness, mantle viscosity, and loading history. The combined GIA estimation exhibited a much better agreement with GNSS-based uplift rates corrected for elastic loading effects (11). The GIA uplift was removed from the SERAC surface elevation change time series (Fig. S3A).

The instantaneous elastic response of the solid Earth is calculated after deriving an estimation of the total mass change. We use the Ice-sheet and Sea-level System Model (ISSM) that allows capturing high-resolution surface mass changes (13). We rely on the Preliminary Reference Earth Model (PREM) and the associated Green's function to solve for the elastic vertical land motion (VLM) and the ratio of mass change to elastic VLM (13). Although the estimated total ice mass change is corrected for firn air content change and GIA, it still contains the elastic VLM signal. Thus, we use the ratio of mass change to elastic VLM and the condition that their sum equals the estimated total mass change in meters of ice to solve for the elastic VLM in response to the actual mass change. We removed outliers by applying a local median filter with a varying searching radius depending on the number of neighbors and a varying threshold of median absolute deviation (MAD) based on the distribution of the neighbors' values. Finally, we re-gridded the filtered elastic VLM to our spatial domain, described in the ice sheet mask section (Fig. S3B).

Firn Height Change Corrections. After removing GIA from the surface elevation change time series, we removed firn height change, i.e. the total height change due to surface processes, to get the residual (Fig. S4). Ignoring elastic VLM and basal melt, this residual is considered "dynamic ice thickness change", which is the ice thickness change related to changes in ice flow (14). The firn height change, modeled by the Firn Densification Model (FDM), includes elevation change due to surface mass balance (SMB) anomalies and firn air content (FAC) change (15–17). FAC-driven elevation change, i.e., resulting from firn density variations, does not contribute to mass change. Previous studies reported a large spread in SMB and FAC from different climate and firn models in the Greenland Ice Sheet (18, 19). Because these climate and firn densification models differ in numerous ways, and each could be advantageous in certain perspectives, we use three different firn height change datasets to examine their impact on mass change reconstruction.

The three firn height change datasets we use are from RACMO2.3p2 and IMAU-FDM v1.2G (15, 20), MERRA-2 and GSFC-FDM v1.2.1 (17, 21), and corrected ERA5 and GEMB v1.0 (16). RACMO2.3p2 is the polar version of the Regional Atmospheric Climate Model. We used its downscaled 1 km monthly surface mass balance output from 1958 to 2021 (20). IMAU-FDM (1957–2020) is a firn densification model forced by RACMO2.3p2 output at 5.5 km resolution, before it is downscaled (15). MERRA-2 (Modern-Era Retrospective analysis for Research and Applications, Version 2) is a global atmospheric reanalysis (21). GSFC-FDM (1980–2022) is based on the community firn model (CFM) and forced at the upper boundary by MERRA-2 outputs (17). It has a horizontal resolution of 12.5 km. GEMB (Glacier Energy and Mass Balance model, 1979–2022) is a column model of surface energy, mass exchange, and firn processes (16, 22). It is on an irregular ISSM mesh and forced by ERA5 output from 1979 to 2022, with surface temperature and downwelling longwave radiation forcing, biased-corrected using RACMO2.3 (23) monthly averages from 1980 to 2015. The details of each model can be found in the original papers. For each ice thickness change time series, we extracted the firn height change time series from the nearest grid cell and resampled it to the epochs in the time series using the nearest neighbor date. This step and the following reconstruction steps were repeated using each of the firn height change datasets.

Temporal Interpolation of Dynamic Ice Thickness Change. After correcting for GIA and firn height change, we obtained the time series of dynamic ice thickness change that is not corrected for the elastic VLM. The dynamic ice thickness change time series keeps the irregular sampling of the original surface elevation change time series. It has a relatively low interannual variability (3, 24). This allows us to interpolate dynamic ice thickness change through temporal gaps of several years, for example, when the gap between ICESat and ICESat-2 is not bridged by the airborne missions. We used the Approximation by Localized Penalized Spline (ALPS) method to interpolate the dynamic ice thickness change into regularly sampled time series with 10-day resolution using $p = 4$ and $q = 3$ (25). Then we resampled it annually using balance years with 1995 spanning September 1, 1994, to August 31, 1995. The annual rate reconstructions at SERAC locations are available from September 1, 1978, to August 31, 2020, for the reconstruction using the IMAU-FDM (Fig. S2) and from September 1, 1981, to August 31, 2022, using the other two.

Ice Sheet Mask and Drainage Basin Mask. To define the ice sheet and separate it from weakly and not-connected ice caps and glaciers, we use an updated version of the CCI ice sheet mask (release 2.0) with strongly connected glaciers and ice caps included (connectivity level CL2) (26, 27). This ice mask is based on Landsat images acquired mostly between 1999 and 2005. We removed the floating ice tongues of a few major tidewater glaciers. In northern Greenland, we used the grounded ice sheet boundary from (28) for Petermann Gletscher, Ryder Gletscher, Hagen Brae, Nioghalvfjerdsfjorden, and Zachariae Isstrom. In Jakobshavn Isbrae in western Greenland, we derived the grounding line of Jakobshavn Isbrae using the 2008/06 DEM (29) from the hydrostatic method. This modified CCI ice sheet mask is used as the spatial domain for reconstructing the Greenland Ice Sheet mass change in this study. To minimize projection distortion in the Greenland Ice Sheet, we use EPSG: 32624 – WGS 84 / UTM zone 24N for our spatial domain, which has a central meridian of 39°W. In the future, a more consistent framework is needed to treat the time-varying ice sheet boundary in mass change reconstructions, especially on tidewater glaciers like Ryder Gletscher and Zachariae Isstrom, where the grounding line has retreated dramatically since the 1990s.

Spatial Interpolation of Dynamic Ice Thickness Change. We obtained annual dynamic ice thickness changes at the locations of the SERAC elevation change time series. Despite limited laser altimetry data in the years without satellite laser altimetry (Fig. S1), the temporal interpolation greatly improved the spatial coverage of the annual dynamic ice thickness change (Fig. S2B). We used Ordinary Kriging with a spherical variogram model to interpolate annual dynamic ice thickness change estimates into 1 km regular grids. We used the best-fitting spherical variogram model in each basin and visually checked for underfitting or overfitting. In addition, 34 time series are removed after a visual examination of extreme values on the interpolated grids, mostly due to the irregular sampling of time series and missed outliers within the time series. We removed the annual dynamic ice thickness change from these time series and repeated the spatial interpolation step to improve the quality of the annual dynamic ice thickness change grids. Due to the altimetry (Fig. S1) and firn height change data availability, the gridded solution is available between September 1, 1994, and August 31, 2020, for the IMAU reconstruction, and September 1, 1994, and August 31, 2021, for the other two.

Estimation of Total Mass Change. We summed the gridded annual dynamic mass change and surface mass balance anomaly to calculate the total mass change for each of our three reconstructions. Surface mass balance is an output of GSFC-FDM and GEMB firn densification models, which are forced by precipitation, air temperature, and other climate model outputs to model the snow and firn processes, including runoff. It's not directly provided as an output of the IMAU-FDM. To be consistent, we use SMB from the downscaled 1km RACMO2.3p2, which has a similar firn module to the IMAU-FDM. Then, we calculated the SMB anomaly by removing the mean SMB over the reference period assumed by each FDM. IMAU-FDM assumes the reference period to be 1960–1979, GSFC-FDM uses 1980–1995, and GEMB uses 1979–1988. Next, we calculated balance-year SMB anomalies from the full-resolution estimates (5-day resolution from GSFC-FDM and GEMB, and monthly resolution from the downscaled RACMO2.3p2) and re-gridded them to our spatial domain using bilinear interpolation. We summed the annual SMB anomaly and dynamic ice thickness change, which was converted to dynamic mass change using the ice density of 917 kg/m3, to estimate total mass change. It is then used as the surface load change to model the elastic response of the solid Earth, as described in the solid Earth corrections section. We removed the elastic VLM from the dynamic ice thickness change grids to get the "real" dynamic ice thickness change grids. Finally, the dynamic mass changes are added up with the surface mass balance anomaly to calculate the total mass change. We calculated mass change over our spatial domain in EPSG: 32624 – WGS 84 / UTM zone 24N projection. We also share the mass change grids that are reprojected to EPSG:3413 – WGS 84 / NSIDC Polar Stereographic North due to its popularity in the ice sheet community.

Reconstruction of Annual Ice Surface Elevation Change. We reconstructed annual elevation change by summing dynamic ice thickness change (pre-elastic VLM correction), firn height change, and GIA. Using three different firn height change datasets, we obtained three sets of annual elevation change at 1 km resolution from September 1, 1994, to August 31, 2020. Meanwhile, we also provide the annual elevation change at locations of the SERAC elevation change time series (Fig. S4). We analyzed the spatial variability of the reconstructed total elevation change from September 1, 1994, to August 31, 2020, by calculating the ratio of ice-sheet or drainage-basin area within discrete elevation change bins (Fig. S5).

Comparison with Mass Change from GRACE

GRACE Mascon Data Processing. We compared the annual altimetry-based mass change reconstructions with the GSFC GRACE Global Mascon Solution, version RL06v02 (41), at a drainage basin scale. This GRACE solution is a 1-arc-degree mascon solution that uses spatial regularization techniques to better delineate land-mass change signals from ocean-mass change signals along coastlines (30, 31). Annual mass changes between successive September estimates were computed for the GRACE mascons to compare with the balance-year altimetry mass change reconstructions (Fig. 4). The entire Greenland land area is covered by 198 mascons (Fig. S8A). The spatial domain of our altimetry-based mass change reconstructions overlaps with 181 mascons (mascons with a darker color in Fig. S8A). To compare only the ice sheet mass change, simply ignoring the non-overlapping 17 mascons is not appropriate. The spatial resolution of GRACE observations is limited to 300-350 km, meaning that any single mascon (approximately 112 km in width) contains signal leakage from the surrounding mascons. The GSFC solution minimizes leakage along coastlines, but leakage between mascons within the continent still exists, including both the leakage among drainage basins and between the ice sheet and peripheral glaciers and ice caps (GICs). We corrected for the leakage between the ice sheet and GICs by first binning an altimetry-based mass change rate (32) over the GICs into the GRACE mascon space (Fig. S8B), then multiplying it with the resolution operator, R, from the mascon estimation system to obtain their contribution to the GRACE mascon solutions (Fig. S8C). The full derivation and explanation of the resolution operator are presented in (31). The R-applied mass change of peripheral glaciers and ice caps at GRACE's resolution was subtracted from the original 198 GRACE mascons (Fig. S8D) to estimate the ice sheet mass change from GRACE (Fig. S8E). Mass change was then calculated for the seven drainage basins used in this study (Fig. S8A).

Altimetry-Based Mass Change Data Processing. To facilitate the intercomparison, we also converted our altimetry-based ice sheet mass change to the mass change in GRACE's grids. We first replaced the GIA model with ICE-6G_D to stay consistent with GRACE processing (33). Then we applied the resolution operator, R, to altimetry-based reconstructions that are binned into mascons (first row in Fig. S9) to approximate the effects of leakage among mascons and between drainage basins. The comparison between the altimetry-based reconstructions from this study and GRACE is done by comparing this R-applied altimetry-based mass change (second row in Fig. S9) with the ice sheet GRACE mass change (Fig. S8E). The ice sheet and drainage basin scale comparisons are shown in Fig. 4B.

Uncertainty Estimation from Formal Error Propagation

Drainage Basin Total Mass Change Uncertainty Estimation. The uncertainty of drainage basin total mass change estimates ($\sigma_{\Delta M,total,basin}$) primarily arises from elevation change measurement uncertainty, uneven sampling of elevation change measurements, uncertainty in estimates of firn air content changes, and viscoelastic solid Earth vertical land motion. Uncertainty in estimates of firn air content changes is included here because of our reconstruction approach: we removed firn height change that includes both SMB anomaly and firn air content change at the beginning and later added back SMB anomaly while calculating total mass change. The drainage basin total mass change uncertainty is estimated using the following equation, assuming these uncertainty components to be independent:

$$\sigma_{\Delta M,total,basin} = \sqrt{\sigma^2_{\Delta M,ALPS,basin} + \sigma^2_{\Delta M,FAC,basin} + \sigma^2_{\Delta M,GIA,basin} + \sigma^2_{\Delta M,ESA,basin}} \tag{1}$$

We use the temporal interpolation error from ALPS (25) (the localized interpolator applied to dynamic ice thickness change time series) with the 95% t-confidence intervals to represent random errors in surface elevation measurements and uneven temporal sampling of the time series, assuming a relatively smooth change in dynamic ice thickness. The ALPS interpolation error of annual dynamic ice thickness change at each SERAC time series location i ($\sigma_{\Delta V,ALPS,point,i}$) is calculated using the ALPS error at the start (September 1) and end (August 31) of each balance year, following:

$$\sigma_{\Delta V,ALPS,point,i} = \sqrt{\sigma^2_{V,ALPS,point,i,start} + \sigma^2_{V,ALPS,point,i,end}} \tag{2}$$

Following equation S5 in (3), we estimated the drainage basin ALPS interpolation volume error ($\sigma_{\Delta V,ALPS,basin}$) from individual dynamic ice thickness change time series ($\sigma_{\Delta V,ALPS,point,i}$) by assuming equal area around each time series using:

$$\sigma_{\Delta V,ALPS,basin} = \sqrt{\sum_{i=1}^{N} (\sigma_{\Delta V,ALPS,point,i} A_i)^2} \tag{3}$$

where N is the number of time series in each basin, A_i is the area around location i. A_i is calculated by dividing the basin area (A_{basin}) by N. Thus, $A_1 = A_2 = A_3 = \cdots = A_N$ and $A_{basin} = \sum_{i=1}^{N} A_i$. The ALPS interpolation error is the highest in the early years when the SERAC surface elevation change time series were relatively poorly sampled. The errors dropped accordingly with improved sampling. Using an ice density of 917 kg/m3 (ρ_{ice}), the drainage basin ALPS interpolation mass change error ($\sigma_{\Delta M,ALPS,basin}$) is calculated as:

$$\sigma_{\Delta M,ALPS,basin} = \rho_{ice} \sigma_{\Delta V,ALPS,basin} \tag{4}$$

The mass change estimation uncertainty from uncertainty in firn air content change ($\sigma_{\Delta M,FAC,basin}$) is calculated as the standard deviation of the three firn air content change datasets (IMAU, GSFC, and GEMB). The uncertainty in GIA at each grid cell is provided by the original study (11). To derive drainage basin mass change uncertainty due to GIA uncertainty ($\sigma_{\Delta M,GIA,basin}$), we first modeled the spatial correlation in the errors using the best-fitting variogram. Then, we approximated the GIA volume error using the spatial covariance of errors, error estimation at each grid cell, and the number of grid cells following equation 18 in (34). Finally, the volume error is converted to $\sigma_{\Delta M,GIA,basin}$ using ice density ρ_{ice}. The mass change uncertainty from uncertainty in the elastic vertical land motion ($\sigma_{\Delta M,ESA,basin}$) is estimated proportionally to the uncertainty of total mass change. First, we calculated the ratio of the drainage basin total mass change to the elastic vertical land motion. Then, we estimated $\sigma_{\Delta M,ESA,basin}$ by multiplying this ratio by the drainage basin total mass change uncertainty that's estimated without considering the error in the elastic vertical land motion in equation 1.

Drainage Basin Dynamic Mass Change Uncertainty Estimation. The uncertainty of drainage basin dynamic mass change estimates has similar components to the total mass change, with uncertainty in firn air content change estimates replaced by firn height change estimates. We estimate the uncertainties from the firn height change estimates ($\sigma_{\Delta M,firn,basin}$) using the standard deviation of the three firn height change datasets (IMAU, GSFC, and GEMB) in each drainage basin. Assuming independent error terms, the uncertainty of annual dynamic mass change in each drainage basin ($\sigma_{\Delta M,dynamic,basin}$) is calculated following:

$$\sigma_{\Delta M,dynamic,basin} = \sqrt{\sigma^2_{\Delta M,ALPS,basin} + \sigma^2_{\Delta M,firn,basin} + \sigma^2_{\Delta M,GIA,basin} + \sigma^2_{\Delta M,ESA,basin}} \tag{5}$$

Ice sheet mass change uncertainty estimation

We estimated ice sheet firn height change error, firn air content change error, and GIA and elastic vertical land motion error following the same strategy as in drainage basins but using the grids of the whole ice sheet. The ice sheet ALPS interpolation error ($\sigma_{\Delta M,ALPS,Greenland}$) is calculated as follows, assuming the ALPS interpolation uncertainty in each basin is independent:

$$\sigma_{\Delta M,ALPS,Greenland} = \sqrt{\sum_{basin \in B} \sigma^2_{\Delta M,ALPS,basin}} \tag{6}$$

where B includes the seven drainage basins used in this study.

Multi-Year Average Mass Change Uncertainty Estimation. We also report the uncertainty of the 5-year and 1994-2020 average dynamic and total mass change for each region (drainage basins and Greenland Ice Sheet) ($\sigma_{\Delta M,Y,region}$). They are derived using the annual errors of dynamic or total mass change, assuming the errors from each year are independent, following:

$$\sigma_{\Delta M,Y,region} = \frac{\sqrt{\sum_{year\in Y} \sigma^2_{\Delta M,year,region}}}{N_Y} \tag{7}$$

where Y is the period of interest, such as 1995 – 2000, and N_Y is the number of years in Y. We acknowledge the potential underestimation of this uncertainty due to the neglect of the autocorrelation of firn air content change and firn height change estimations. We also ignored uncertainty from basal melt (35), considering the complex relationship between basal melt and surface elevation change.

Uncertainty Estimations from Two Different Approaches. The formally propagated errors derived using the method described above, and the spread of mass change that's calculated as the standard deviation of our three reconstructions using different firn height change datasets, are shared in the dataset Uncertainty_annual_mass_change_basins.xlsx. The error components contributing to the error from formal error propagation, such as ALPS interpolation error, are shared in the dataset Formal_uncertainty_components_basins.xlsx.

In general, the annual uncertainty estimation from formal error propagation is of the same magnitude as the uncertainties represented by the standard deviation of the three reconstructions using different FDMs. We notice that for the dynamic mass change errors, the standard deviation of the three reconstructions is relatively consistent and autocorrelated temporally, impacted by the smoothing effect of the temporal interpolation technique we used. On the other hand, the spread in firn height change estimations has a significant impact on dynamic mass change errors estimated from formal error propagation. Despite the efforts to formally propagate errors, it's still under numerous assumptions and is hard to be comprehensive, considering the complexity of each dataset and reconstruction steps. Therefore, in the main text, figures, and tables, we reported the spread of mass change that can be interpreted more straightforwardly.

Figures

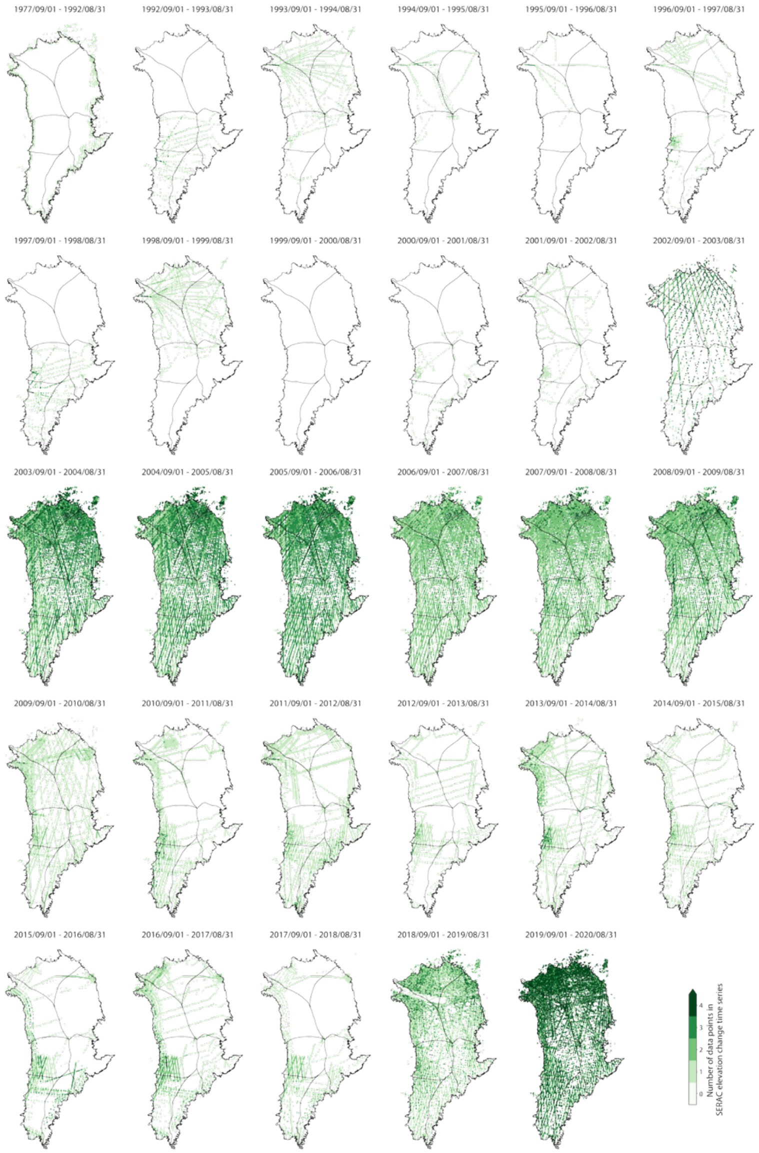

Fig. S1. Number of observational periods (epoch) during each balance year in the SERAC surface elevation change time series. Using the SERAC algorithm, one elevation is obtained at each epoch at the centroid of the 1 km2 patch using all observations within the patch. The first map, dated 1977/09/01–1992/08/31, shows the locations of SERAC time series that includes the aerial photographs (1978–1987) (7). Between 1993 and 2002, the spatiotemporal sampling of the SERAC time series was driven by the observations acquired by the Airborne Topographic Mapping system (ATM). The spatial coverage increased after ICESat was launched in 2003. Between 2009 and 2019, the Operation IceBridge mission, including the ATM and LVIS data acquisitions, was used to bridge the gap between ICESat and ICESat-2. ICESat-2, which was launched in 2018 and is still operating, improved the temporal sampling of elevation change observations. Note that the SERAC time series locations on these maps do not reflect all the flight lines and satellite ground tracks, as they are primarily determined by ICESat/ICESat crossovers or ICESat and ATM/LVIS overlap to obtain extended time series.

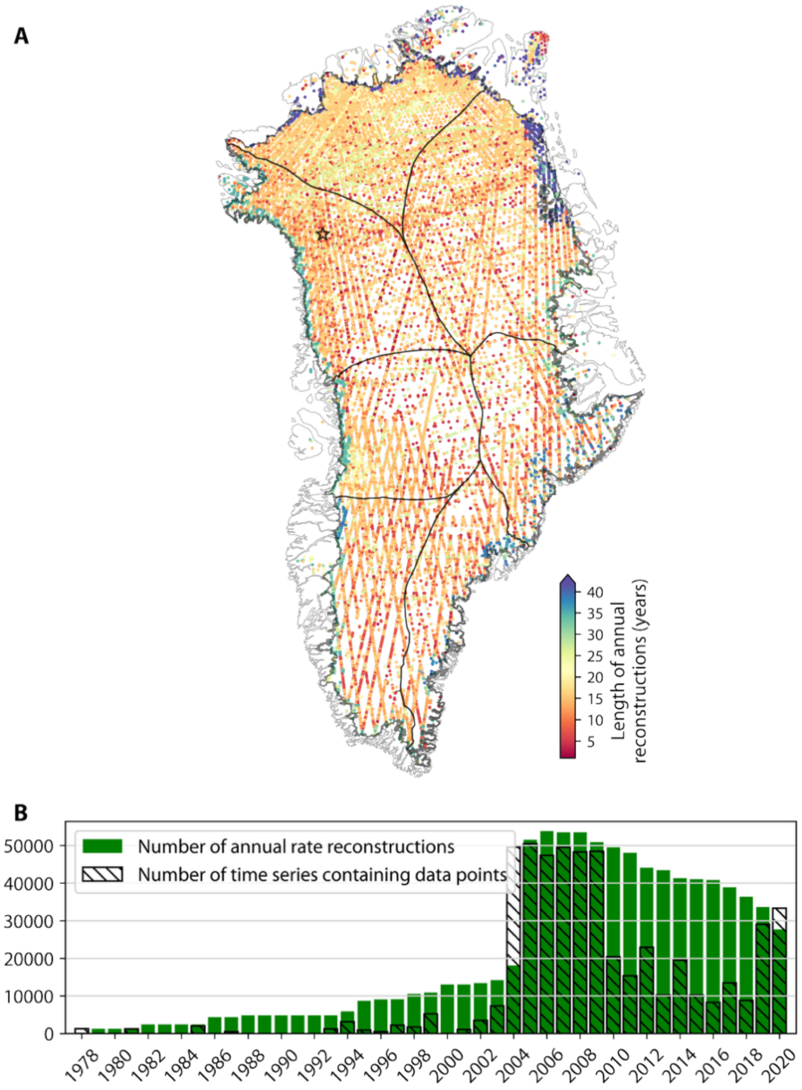

Fig. S2. Annual reconstruction statistics. (A) Points indicate the locations of SERAC elevation change time series. They are colored by the length of the annual dynamic mass change or elevation change reconstructions for the 1978–2020 balance years. The black star in NW marks the location of the SERAC time series in Fig. S4. (B) The green bars are the number of annual rate reconstructions in each balance year. These annual rates are derived after the temporal interpolation of the dynamic ice thickness change time series, which has the same irregular sampling as the SERAC elevation change time series. Bars filled with backslashes represent the number of SERAC time series that have elevation reconstruction data points in each balance year. The number of annual rate reconstructions increases after new observations become available. For example, the largest increase in the number of annual rate reconstructions happened from 2004 (2003/09/01–2004/08/31) to 2005 (2004/09/01–2005/08/31), after the dramatic improvement of data availability from ICESat in the 2004 balance year. Temporal interpolation greatly increased the number of annual rate reconstructions before 2003 and between 2010 and 2019, when satellite laser altimetry measurements were unavailable.

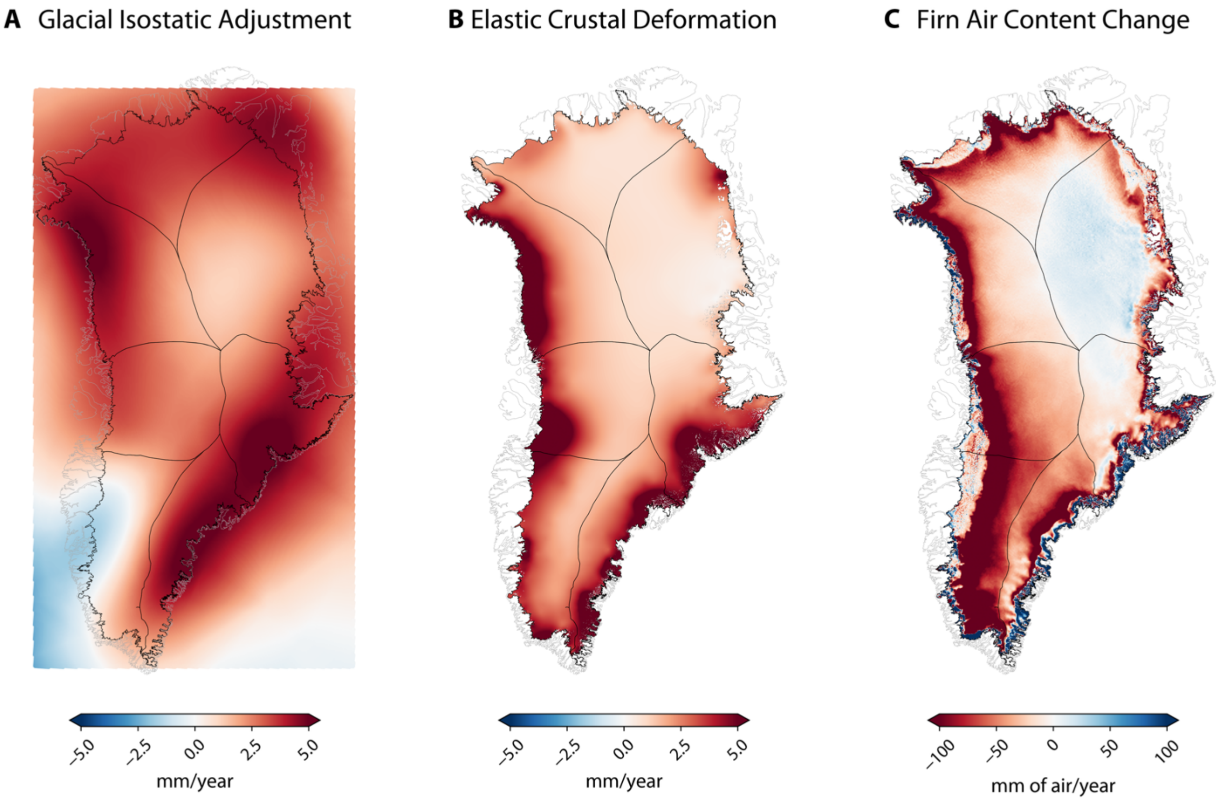

Fig. S3. Processes contributing to surface elevation change but not to ice mass change. (A) Glacial Isostatic Adjustment (GIA) rate, including the GIA in response to the post-Medieval Warm Period (MWP) deglaciation (10, 11). (B) Mean annual elastic crustal deformation between 1994/09/01 and 2020/08/31 (using mass change reconstruction with GSFC-FDM as surface load change from this study). (C) Mean annual firn air content change from the GSFC-FDM between 1994/09/01 and 2020/08/31. Positive values in A and B indicate land uplift. Note the different scales for color bars in A, B vs. C.

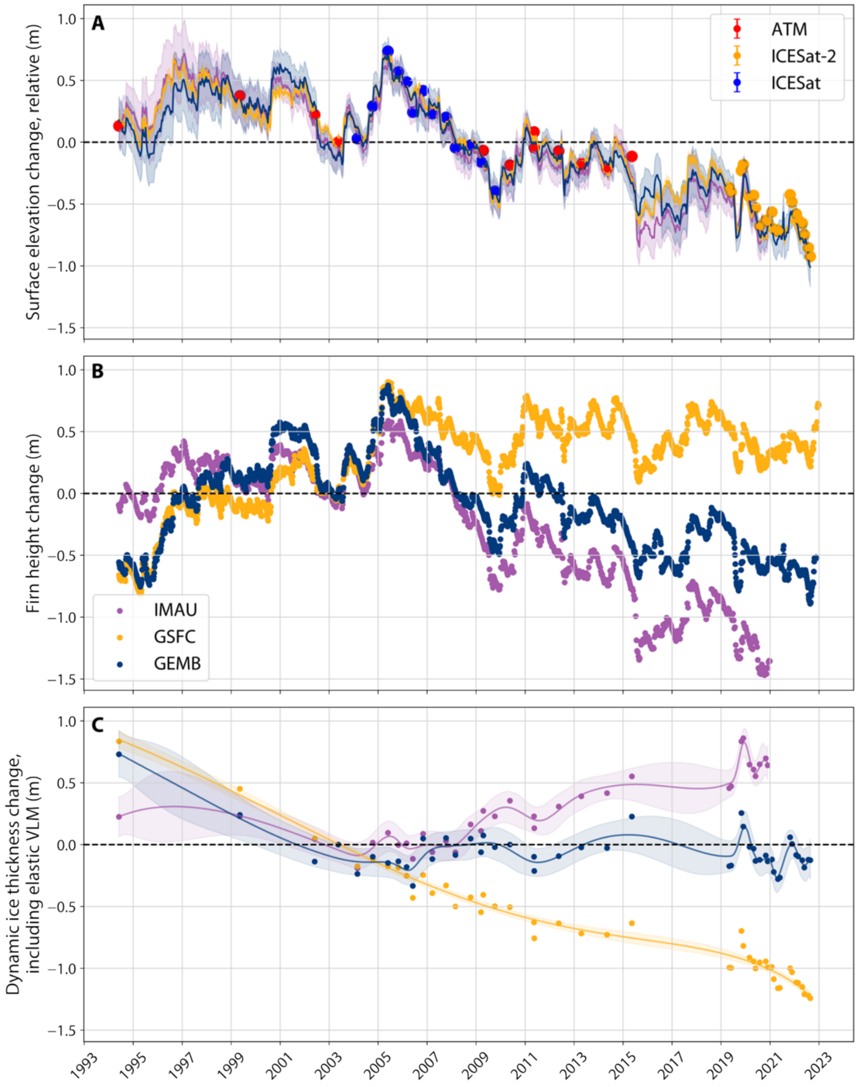

Fig. S4. Detailed reconstruction of ice sheet elevation changes calculated from interpolated ice dynamics and modeled firn height changes due to surface processes. The time series location is marked as a black star in figs. S2 and S11. Metadata about this SERAC elevation change time series is included in Table S3. (A) Surface elevation change. Points are the relative surface elevations from SERAC, colored according to the sensors. Lines with different colors show high-temporal resolution elevation change time series calculated by adding together the interpolated dynamic ice thickness change (10-day resolution) in C with full-resolution firn height change time series (5-day resolution for GSFC and GEMB and 10-day for IMAU) in B from different FDMs. (B) Firn height changes from different FDMs. (C) Dynamic ice thickness change after removing GIA and firn height change from the surface elevation change time series in A are shown as points. Solid lines are the interpolated results using ALPS with p = 4 and q = 3 (25). This location has a total uplifting of ~0.126 m from GIA and ~0.092 m from the elastic VLM between 1994 and 2020. This time series is an extension of the time series in Fig. 11 in (25), where more details about the method can be found. Shading in A and C shows the 95% confidence interval from ALPS interpolation.

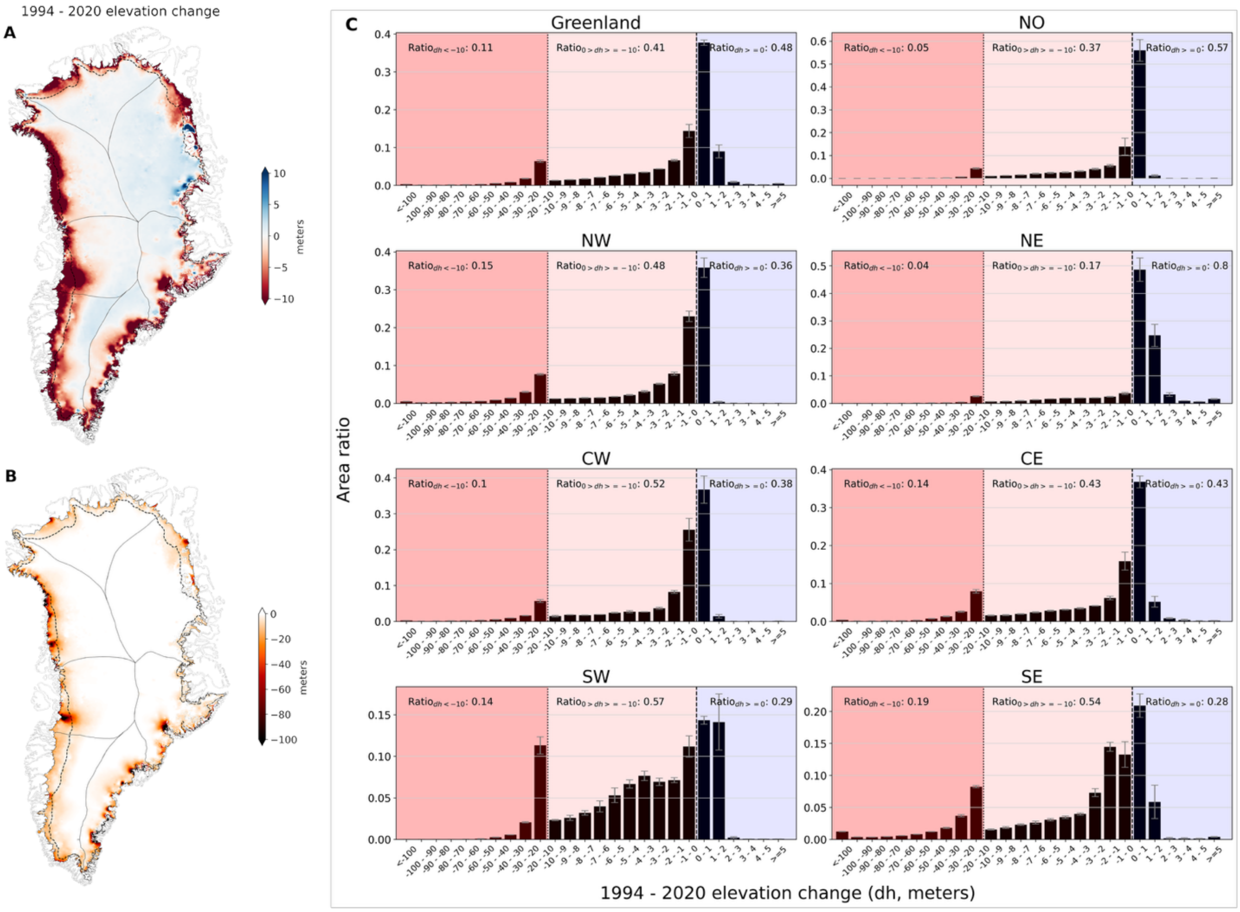

Fig. S5. Total surface elevation change of the Greenland Ice Sheet from September 1, 1994, to August 31, 2020. (A) Map of reconstructed 1994/09/01–2020/08/31 cumulative elevation change, average from our three reconstructions. (B) Same as A but with a color scale ranging from -100 to 0 meters, emphasizing the rapid thinning near the tidewater glacier termini. Drainage basin outlines and the 1994 - 2020 ELA are shown as black solid and dashed lines, respectively. (C) Area ratio of each elevation change group relative to the total area of each region. This is based on the average of our three elevation change reconstructions with different FDMs. The error bars represent the standard deviation of the three. The bin size of the elevation change group is set to be 1 m between -10 m and 5 m, 10 m between -100 m and 10 m, and those less than -100 m or greater than 5 m are summed. The area ratios of thinning greater than 10 m, thinning less than 10 m, and thickening of each region are reported on the corresponding panel.

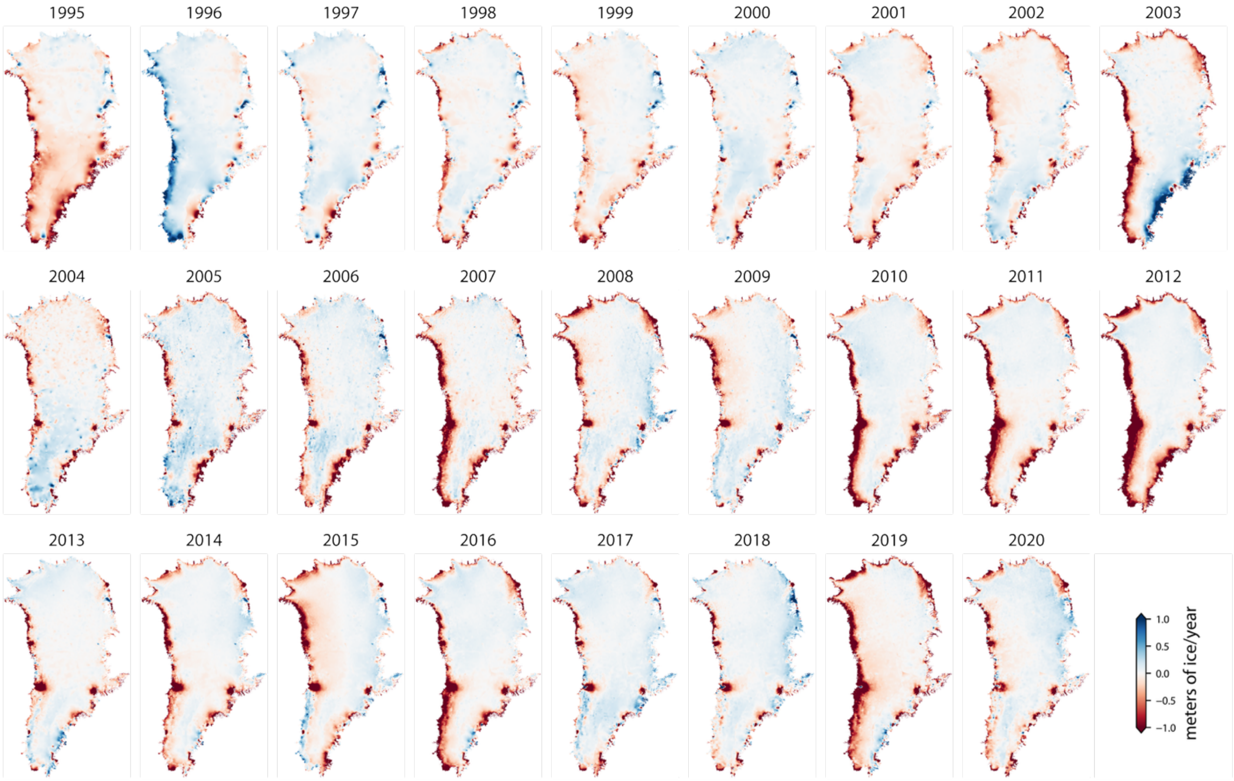

Fig. S6. Maps of annual mass change rates of the Greenland Ice Sheet. Annual balance year mass change rates are averaged over our three reconstructions. The unit of the maps is meters of ice/year with the ice density of 917 kg/m3.

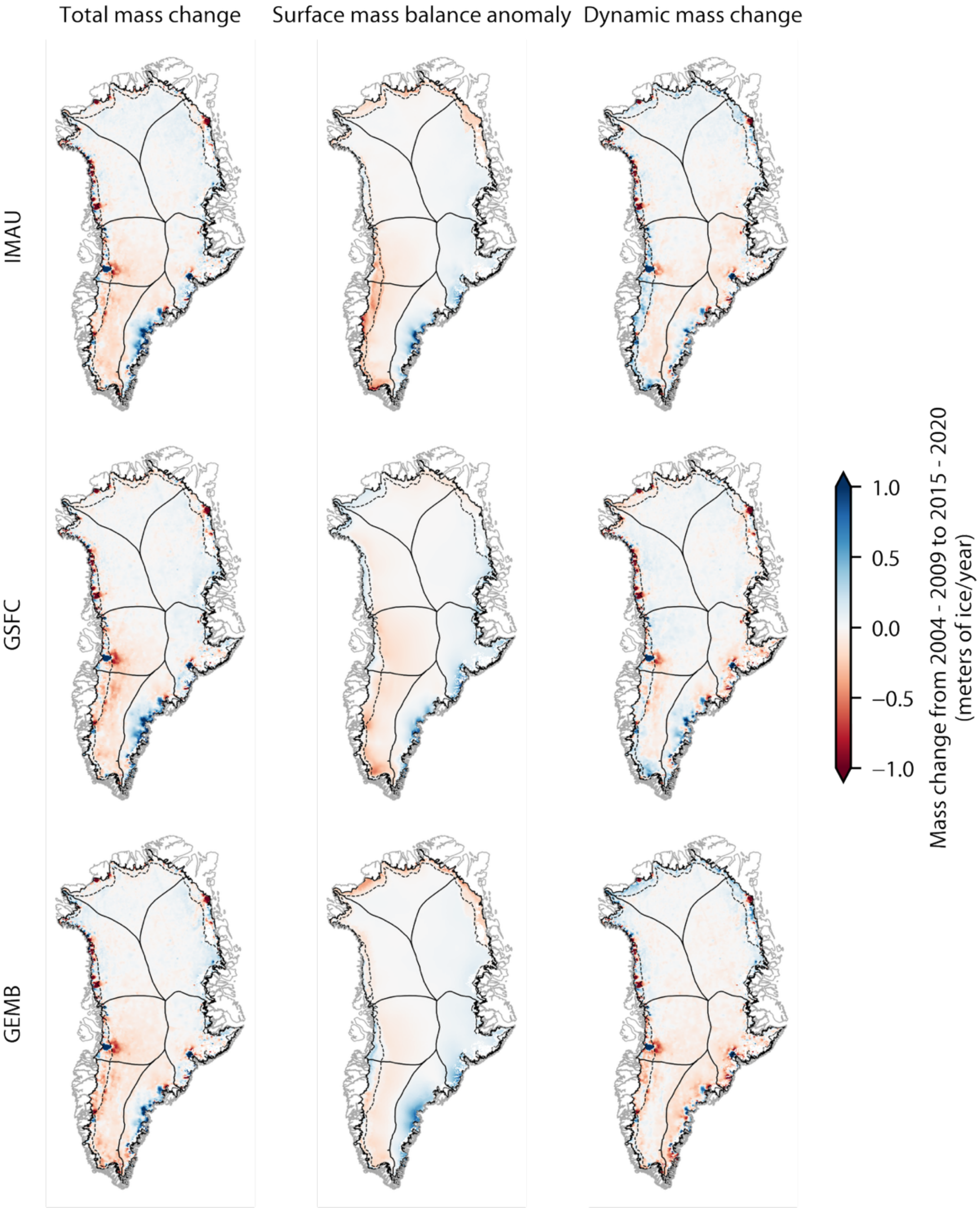

Fig. S7. Total, surface, and dynamic mass change rates from 2003/09/01 - 2009/08/31 (2004 - 2009) to 2014/09/01 - 2020/08/31 (2015 - 2020) using the different FDMs. Similar to the middle map in Fig. 3, the red color on the map indicates increasing mass loss or decreasing mass gain between 2014–2020 compared to 2003–2009, and vice versa.

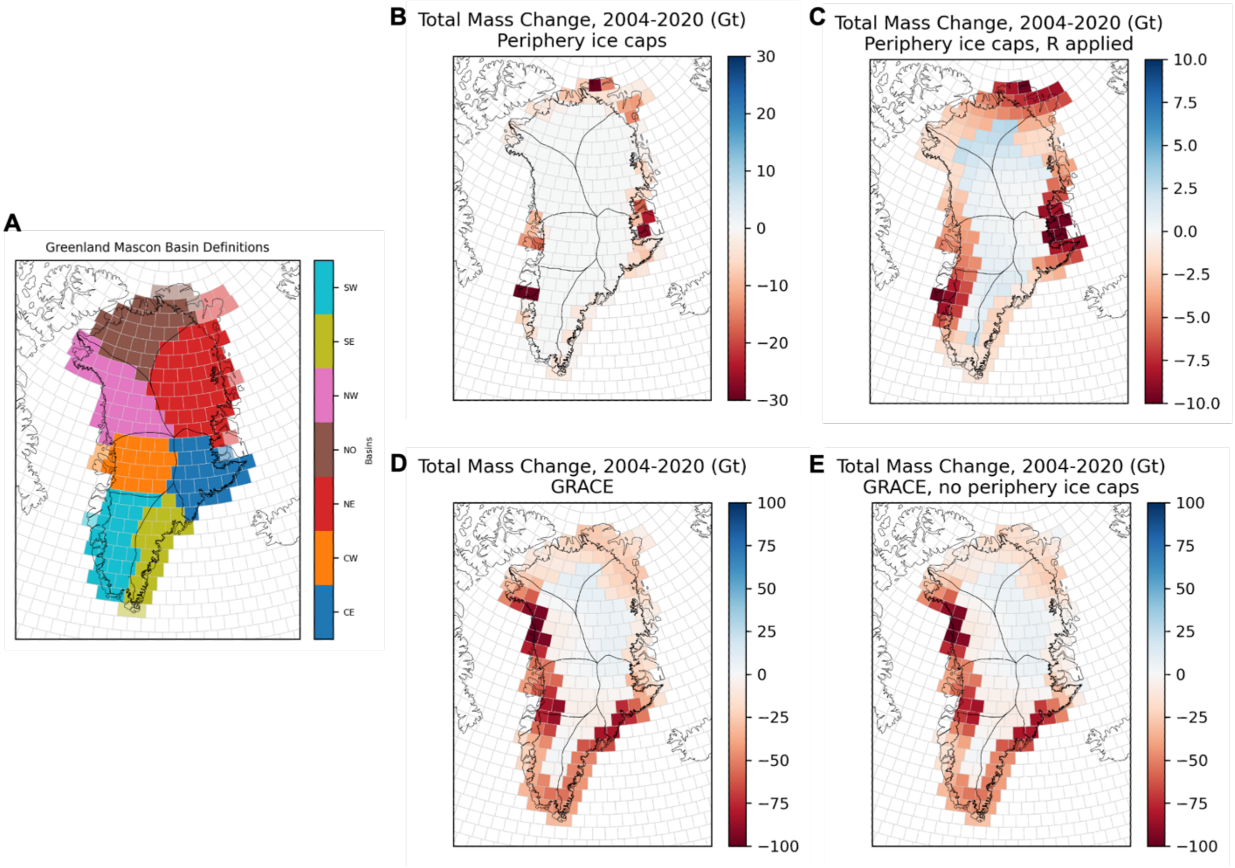

Fig. S8. Mass change from GRACE without peripheral glaciers and ice caps. (A) GRACE mascons and the drainage basin they are assigned to. The light color shows the assigned drainage basins of mascons outside the ice sheet boundary. (B) Mass change of peripheral glaciers from (32) that's binned into GRACE mascons for the balance years 2004 – 2020 (September 1, 2003 – August 31, 2020). (C) Mass change of peripheral glaciers after applying the resolution operator, R. (D) Mass change from GRACE mascon solution, including ice sheet and peripheral glaciers and ice caps. (E) Greenland Ice Sheet's mass change from the GRACE mascon solution without peripheral glaciers and ice caps. E is derived by removing C from D. Drainage basin mass change from GRACE is calculated using the mascons in A, including those outside the ice sheet boundary that contain mass change leaked from the ice sheet. Note the different color bars in panels B-E.

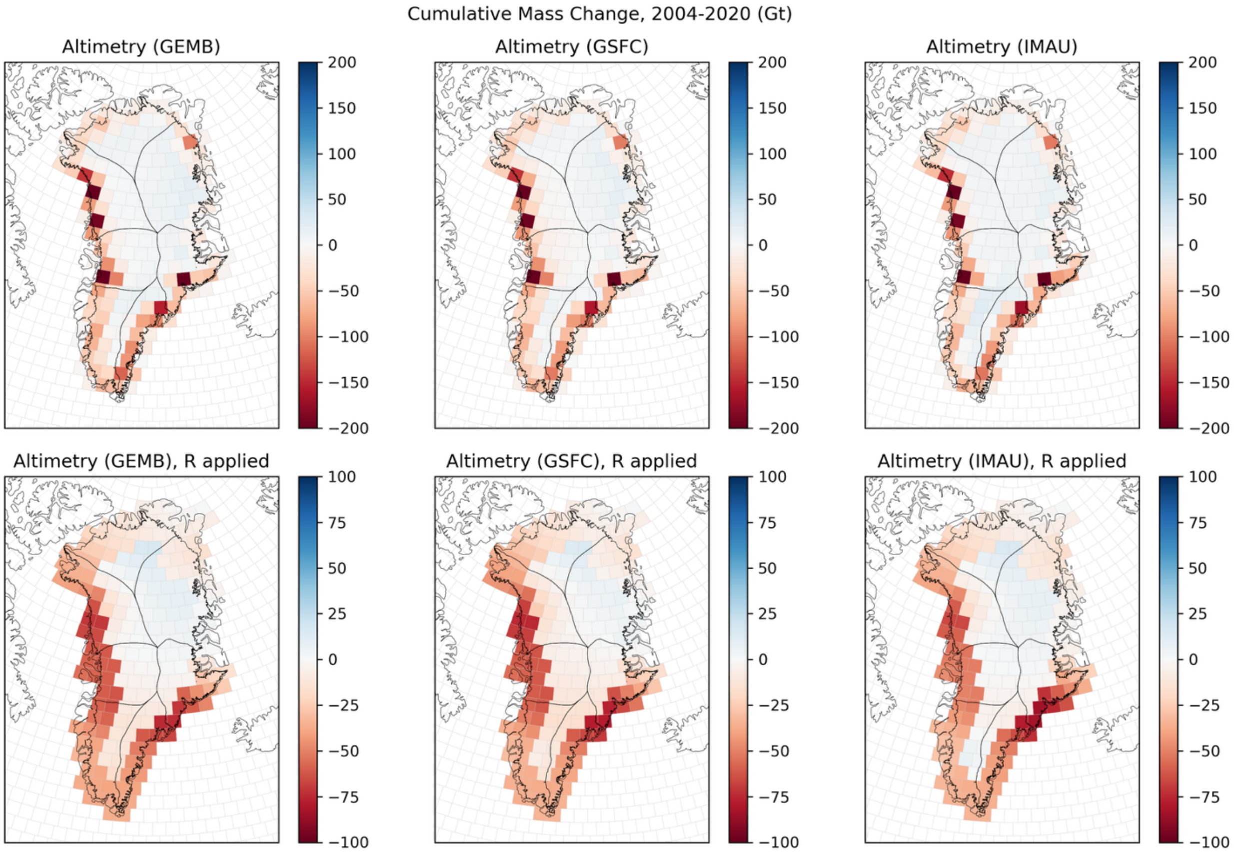

Fig. S9. Altimetry-based mass change at GRACE's resolution. The first row shows laser altimetry-based mass change reconstructions using different FDMs for the balance years 2004 – 2020 (September 1, 2003 – August 31, 2020), which are binned into the GRACE mascon space. The GIA is switched to ICE_6G-D, used by the GRACE solution. The second row shows the result of applying the resolution operator R to the first row to simulate altimetry-based mass change as seen by GRACE.

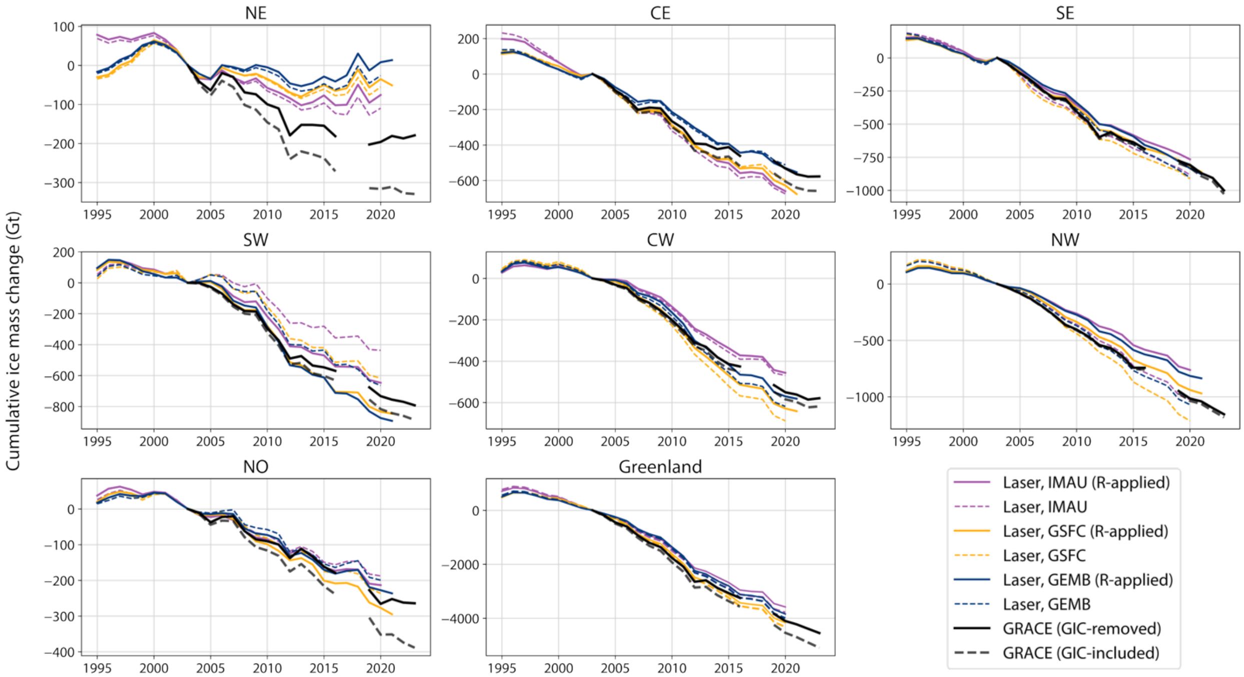

Fig. S10. Cumulative mass change from laser altimetry with different FDMs and GRACE. In addition to the comparison in Fig. 4, colored dashed lines show the original laser altimetry-based reconstructions from this study (before applying R) and the ice sheet plus peripheral glaciers and ice caps (GIC) GRACE solution (Fig. S8D) in each region.

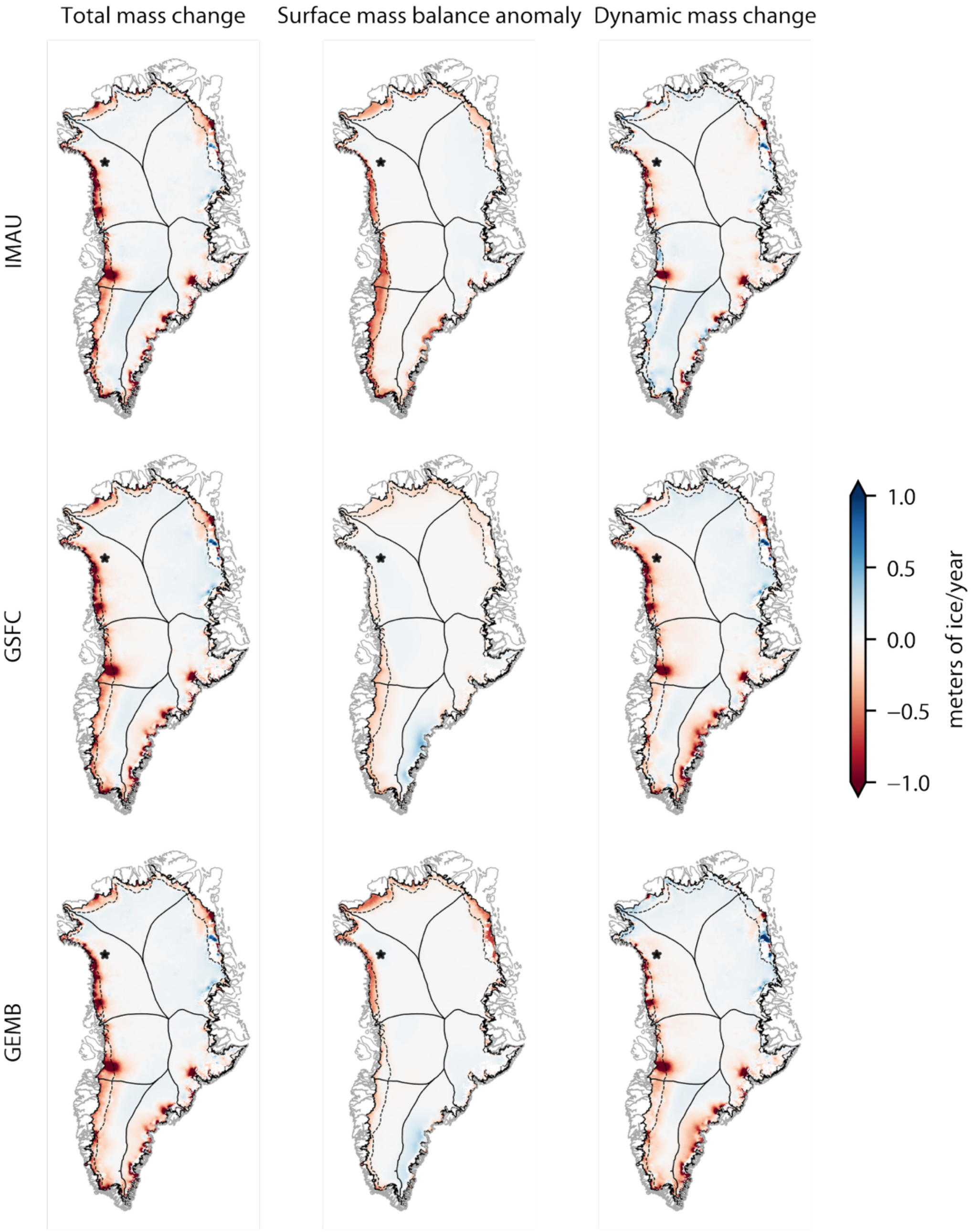

Fig. S11. Partitioned Greenland Ice Sheet mass change rate from laser altimetry with different FDMs between 1994 and 2020. The black star in NW marks the location of the SERAC time series in Fig. S4.

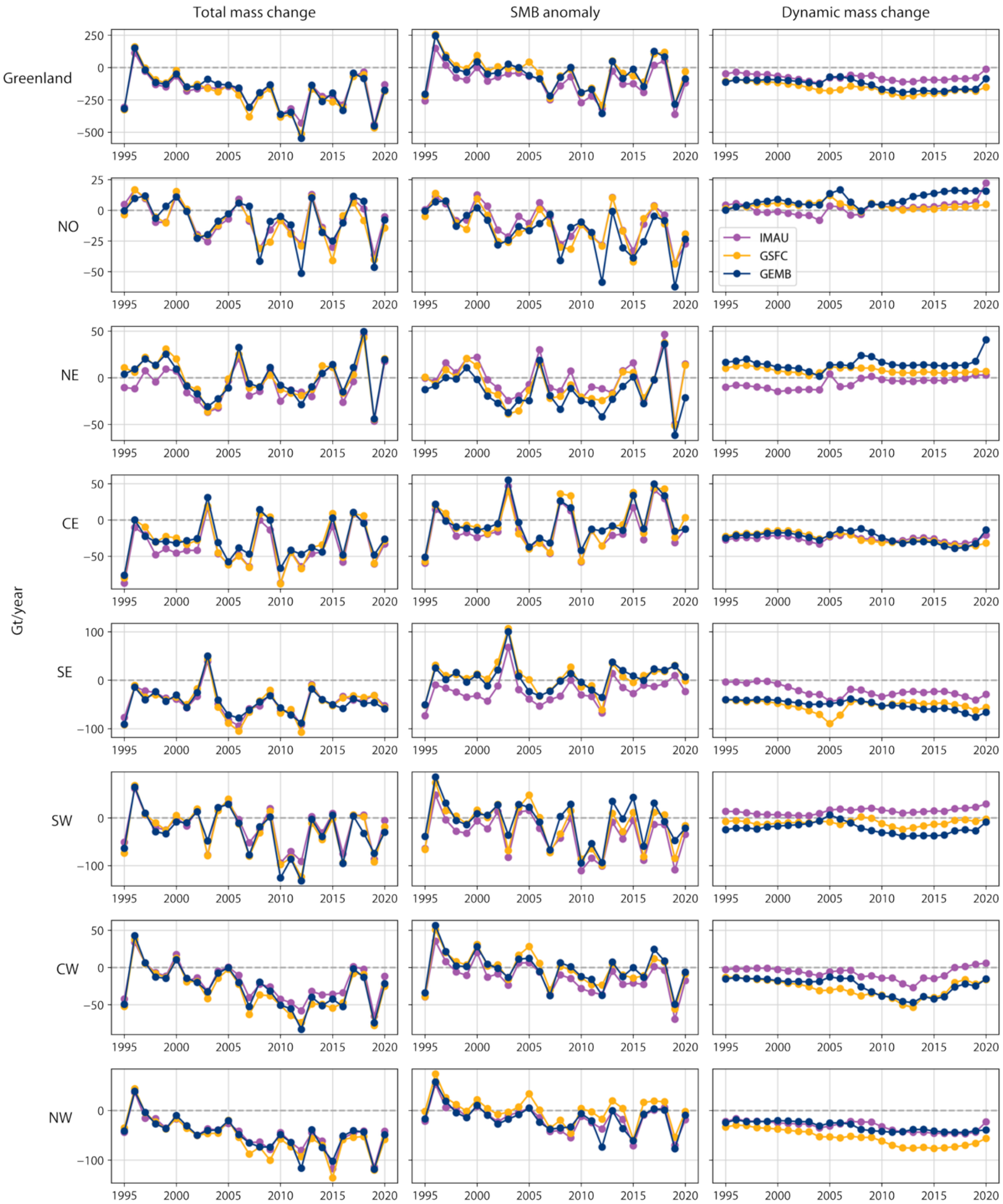

Fig. S12. Annual partitioned mass change rates in each region from using different FDMs. Annual total, surface, and dynamic mass change from using three different FDMs: purple (IMAU-FDM), orange (GSFC-FDM), and blue (GEMB). The rates are in gigaton of ice per year.

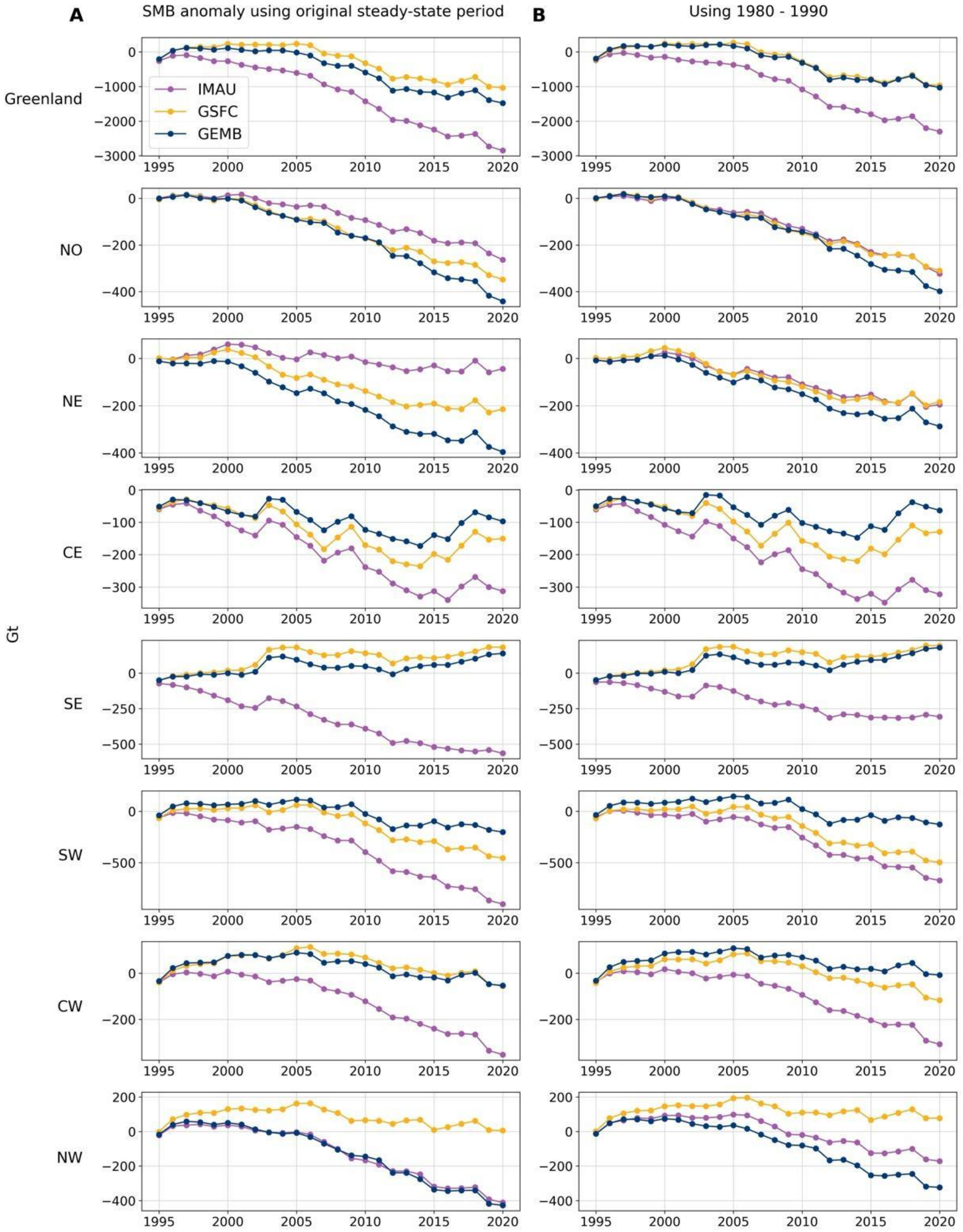

Fig. S13. Cumulative SMB anomaly calculated using different assumptions of the steady-state period. (A) SMB anomalies in the Greenland ice sheet and each drainage basin from using their original steady-state period assumptions: IMAU-FDM (purple): 1960 - 1979, GSFC-FDM (orange): 1980 - 1995, and GEMB (blue):1979 - 1988. (B) SMB anomaly recalculated assuming a common steady-state period of 1980-1990.

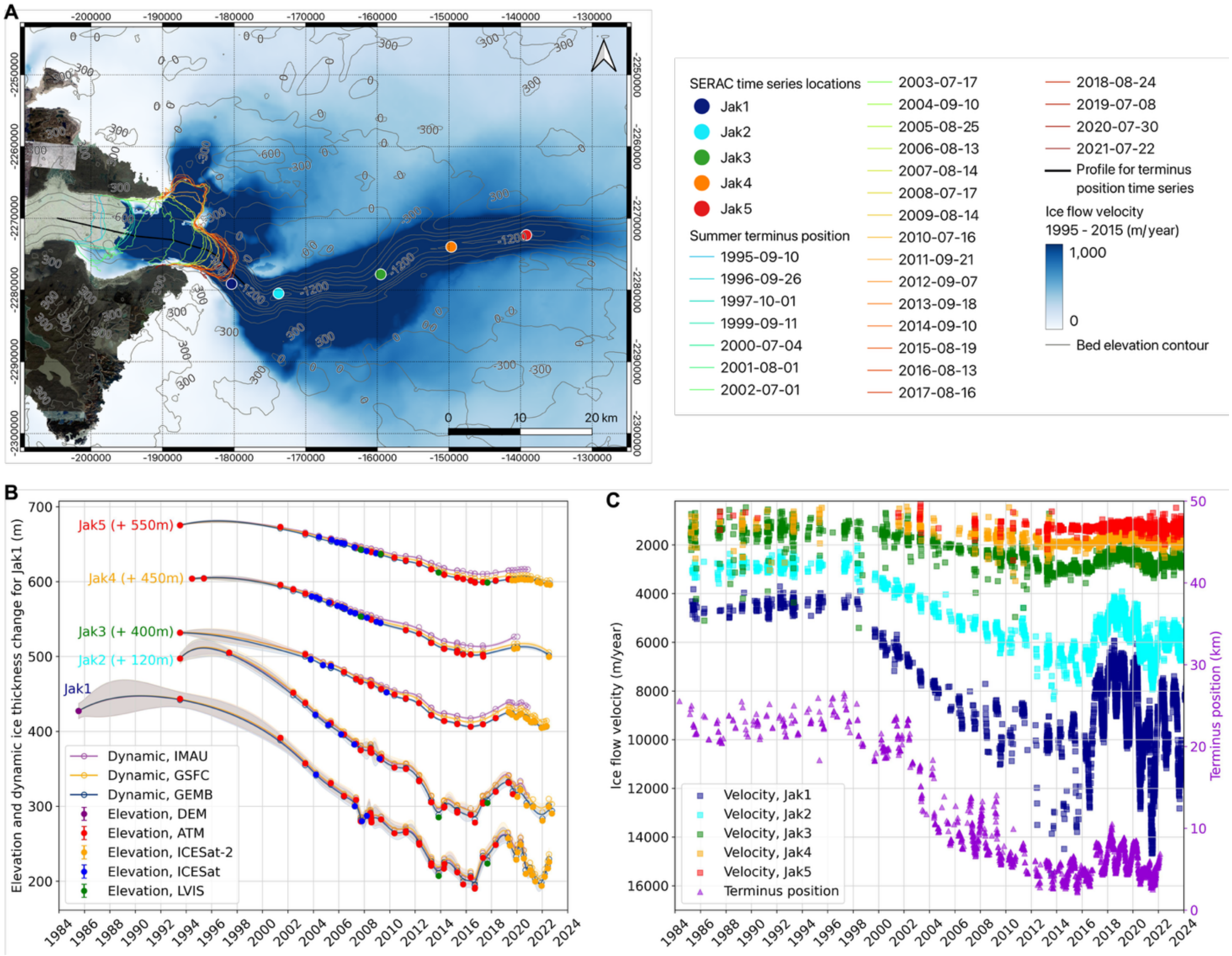

Fig. S14. Propagation of dynamic ice thickness changes upstream in the Jakobshavn Isbrae drainage basin. (A) Locations of the five SERAC time series shown in B along the deep trough of Jakobshavn Isbrae in CW Greenland, with Jak1 being the closest to the terminus and Jak5 being the furthest. Jak1 is the time series of Jakobshavn Isbrae shown in Fig. 6. Metadata about these five SERAC time series is included in Table S3. The basemap is the surface ice flow velocity mosaic (36), overlaid by the summer terminus position since 1995 from AutoTerm (37) and TermPicks (38), and the 300 m-interval bed elevation contours (39). (B) SERAC time series of surface elevation change and dynamic ice thickness changes before elastic VLM correction with different FDMs. The y-axis shows the surface elevation at Jak1, while the other four time series are shifted. The actual elevation at Jak2 is the y-axis value plus 120 m, Jak3 is the y-axis value plus 400 m, Jak4 is the y-axis value plus 450 m, and Jak5 is the y-axis value plus 550 m. See Fig. 6 for details. (C) Surface ice flow velocity time series from ITS_LIVE (40) at the locations of SERAC time series, and terminus position time series along the black profile on A. Downward trends in the time series indicate thinning, acceleration, and retreat.

(1) Docker Smith Gletscher W, NW

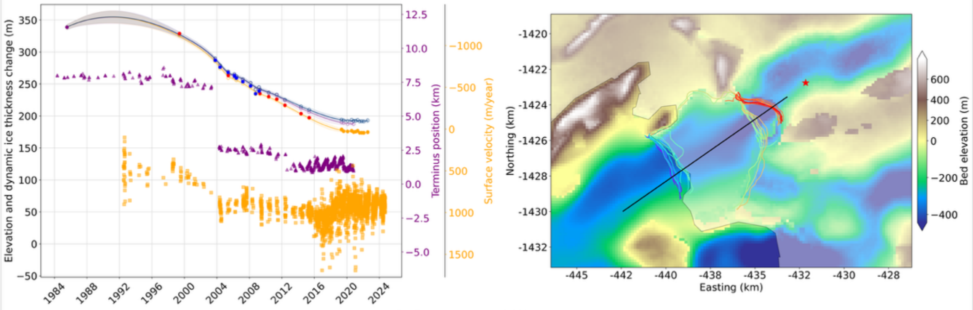

(2) Dietrichson, NW

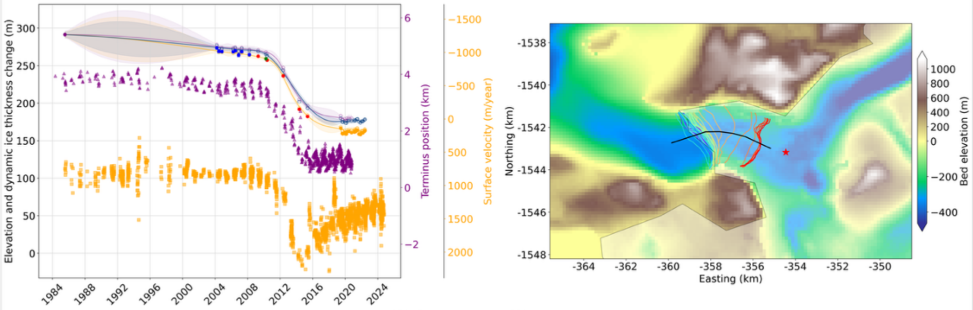

(3) Steenstrup, NW

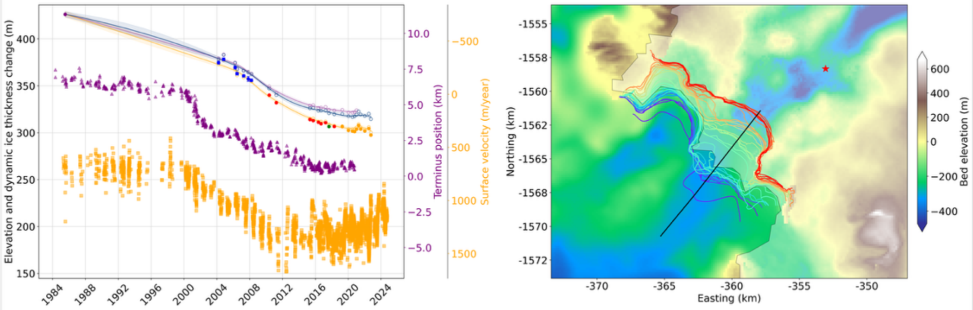

(4) Kakivfaat Sermiat, NW

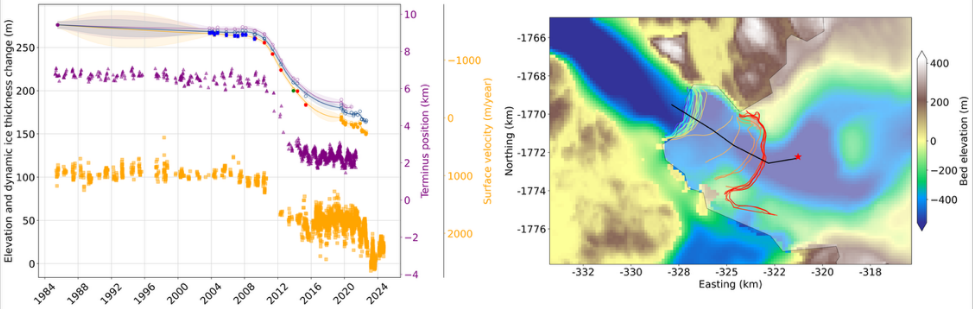

(5) Jakobshavn Isbrae, CW

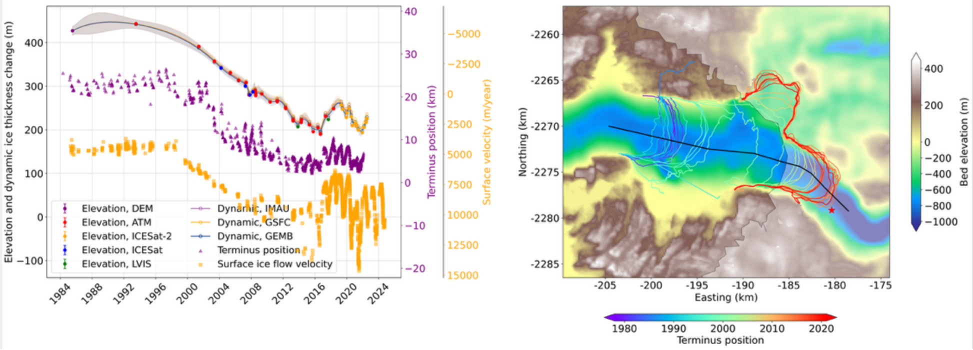

Fig. S15. Decadal changes in ice thickness, velocity, and terminus position of selected tidewater glaciers in western Greenland. The time series figures on the left show the time series of surface elevation change from SERAC, dynamic mass change calculated using different FDMs, terminus position time series (37, 38) along the black profile on the bed elevation map, and ice flow velocity (40) at the same location as the SERAC time series. Downward trends in the time series indicate glacier thinning, retreating, and accelerating. The maps on the right show the bed elevation (39) near the terminus of each glacier. The red star marks the location of the SERAC and ice flow velocity time series. The most retreated terminus position of June to October in each year is overlaid on the bed elevation map. The white shaded area marks where the ice sheet is using the drainage basin outline in (41).

(6) Zachariae Isstrom, NE

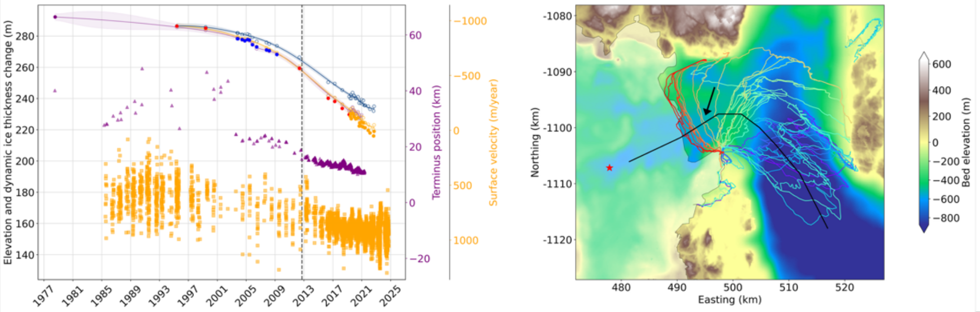

(7) Kangerlussuaq, CE

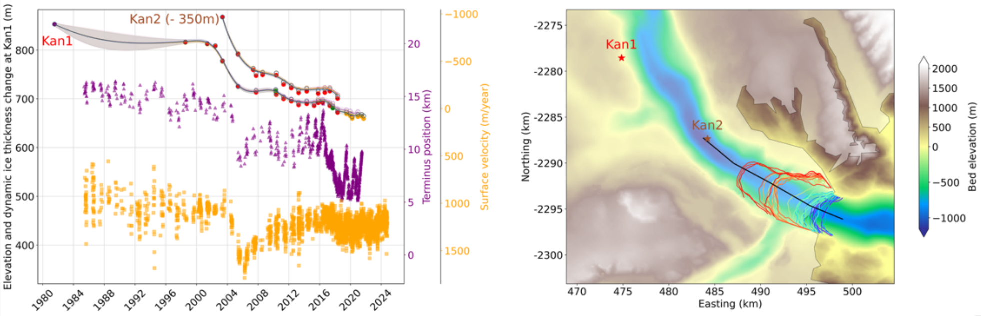

(8) Helheim Gletscher, SE

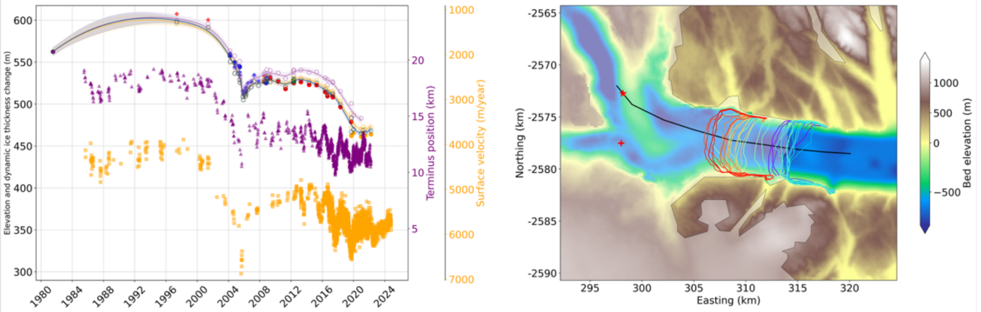

(9) Ikertivaq NN, SE

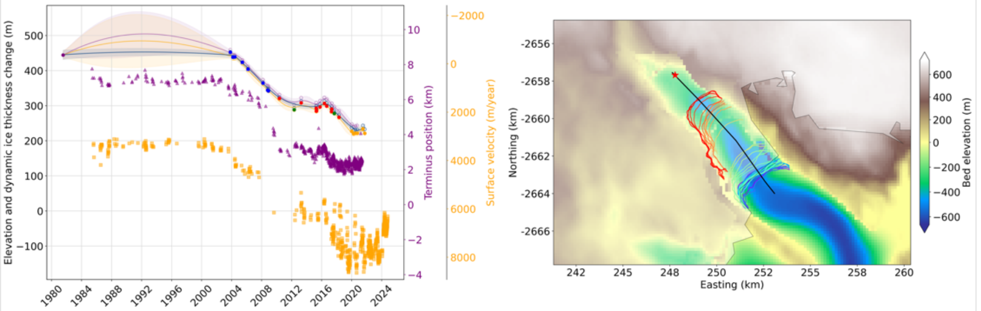

(10) Tingmiarmiut Fjord, SE

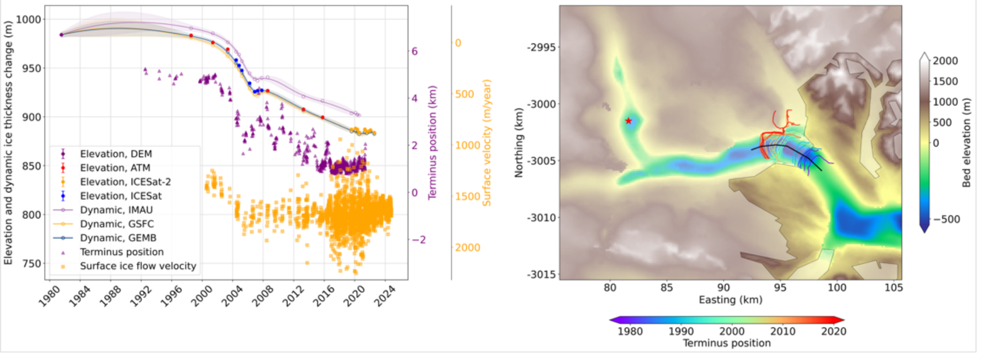

Fig. S16. Decades of observations of selected tidewater glaciers in eastern Greenland. Same as Fig. S15, but for selected glaciers in eastern Greenland. In the time series figure of Zachariae Isstrom, the black dashed line indicates 2012/09/12. The black arrow on the bed elevation map points to the calving front location on this date, when the glacier has retreated into the main trunk. A supplementary set of elevation and dynamic ice thickness change time series, Kan2, is added for Kangerlussuaq. For Helheim Gletscher, the supplementary data points from another time series located at the red plus marker on the bed elevation map are shown as plus markers in the time series.

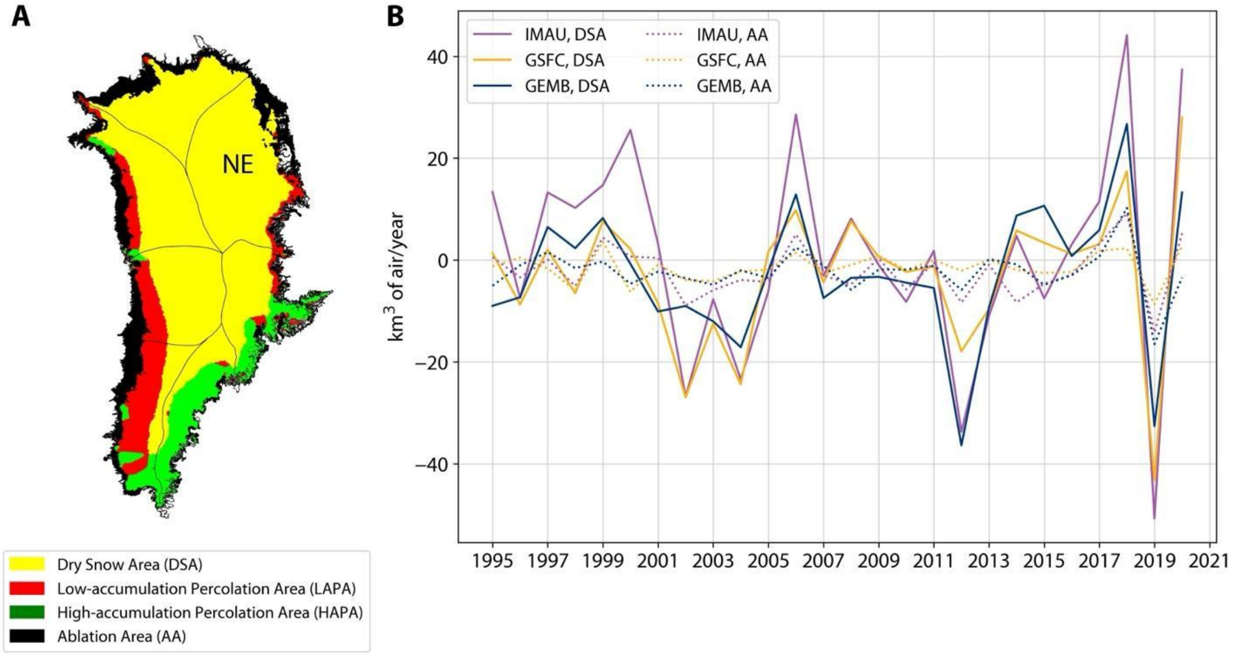

Fig. S17. Annual firn air content (FAC) changes in the ablation area (AA) and dry snow area (DSA) of NE from different FDMs. (A) Following (42), we divided the Greenland ice sheet into 4 climate zones: Dry snow area (DSA, yellow), low accumulation percolation area (LAPA, red), high accumulation percolation area (HAPA, green), and ablation area (AA, black). (B) The annual firn air content change in DSA and AA of NE from the three FDMs used in this study.

Tables

Table S1. Comparison of Greenland Ice Sheet mass change reconstructions with other studies. The mass changes from this study are the average of three reconstructions that use different FDMs. The uncertainty value represents the standard deviation of these three reconstructions. The IMBIE3 estimate is derived from altimetry, GRACE gravity, and input-output methods. Most mass change rates are reported directly in the cited literature. For the time spans marked by an asterisk (*), we recalculated the mass change based on the monthly or annual values provided in the datasets using the overlapping period with this study.

Study	**Method**	**Time span**	**Mass change (Gt/year)**	**Time span (this study)**	**Mass change (this study; Gt/year)**
Csatho et al. (2014) (3)	Laser altimetry	2003/09/01–2009/08/31	-243 ± 18	2003/09/01–2009/08/31	-194 ± 17
Otosaka et al. (2023) (43)	IMBIE3 reconciled	1994/09/01–2020/08/31*	-179 ± 16	1994/09/01–2020/08/31	-191 ± 6
Khan et al. (2022) (44)	Laser and radar	2011/04–2020/04	-273 ± 17	2011/09/01–2020/08/31	-240 ± 15
Simonsen et al. (2021) (45)	Radar altimetry	1994–2020*	-167	1994/09/01–2020/08/31	-191 ± 6
Smith et al. (2020) (46)	Laser altimetry	2003/2008–2018/2019	-200 ± 12	2003/09/01–2019/08/31	-242 ± 13
Mouginot et al. (2019) (41)	Input-output method	1994.5–1999.5*	-54	1994/09/01–1999/08/31	-88 ± 10
Mouginot et al. (2019) (41)	Input-output method	1999.5–2009.5	-187 ± 17	1999/09/01–2009/08/31	-165 ± 12
Mouginot et al. (2019) (41)	Input-output method	2009.5–2018.5	-286 ± 20	2009/09/01–2018/08/31	-251 ± 14

Table S2. Greenland Ice Sheet surface mass balance anomaly (surface mass change) and dynamic mass change from 1994 to 2020. Mean annual mass change rates of our three reconstructions with different firn densification models every five years since 1995, as well as from 1994 to 2020. The uncertainty represents the standard deviation of the three reconstructions. The rates are in gigaton of ice per year.

Region	**Mean surface mass balance (SMB) anomaly (Gt/year)**					
	1995/09/01-2000/08/31	**2000/09/01-2005/08/31**	**2005/09/01-2010/08/31**	**2010/09/01-2015/08/31**	**2015/09/01-2020/08/31**	**1994/09/01-2020/08/31**
Greenland	51 ± 38	-31 ± 28	-130 ± 24	-127 ± 27	-75 ± 34	-69 ± 30
NE	6 ± 5	-21 ± 6	-9 ± 5	-11 ± 7	-8 ± 6	-8 ± 6
CE	-4 ± 4	-6 ± 4	-14 ± 3	-8 ± 5	6 ± 4	-7 ± 4
SE	0 ± 17	14 ± 17	-16 ± 11	-10 ± 12	7 ± 12	-3 ± 13
SW	12 ± 12	1 ± 10	-37 ± 9	-33 ± 14	-35 ± 13	-20 ± 11
CW	18 ± 6	1 ± 6	-12 ± 5	-16 ± 5	-14 ± 6	-6 ± 5
NW	17 ± 6	-4 ± 8	-26 ± 6	-27 ± 11	-12 ± 8	-11 ± 8
NO	1 ± 1	-15 ± 4	-15 ± 2	-22 ± 5	-19 ± 4	-14 ± 3

Region	**Mean dynamic mass change (Gt/year)**					
	1995/09/01-2000/08/31	**2000/09/01-2005/08/31**	**2005/09/01-2010/08/31**	**2010/09/01-2015/08/31**	**2015/09/01-2020/08/31**	**1994/09/01-2020/08/31**
Greenland	-84 ± 24	-118 ± 26	-116 ± 36	-164 ± 45	-134 ± 45	-122 ± 34
NE	5 ± 11	2 ± 8	8 ± 9	5 ± 7	8 ± 8	6 ± 9
CE	-20 ± 3	-23 ± 3	-22 ± 4	-29 ± 2	-32 ± 2	-25 ± 1
SE	-30 ± 18	-47 ± 16	-42 ± 10	-43 ± 13	-50 ± 15	-42 ± 14
SW	-7 ± 12	-3 ± 8	-2 ± 15	-14 ± 20	-3 ± 19	-6 ± 15
CW	-11 ± 7	-17 ± 8	-23 ± 10	-35 ± 12	-16 ± 11	-20 ± 9
NW	-25 ± 6	-33 ± 9	-39 ± 12	-53 ± 15	-51 ± 12	-40 ± 11
NO	4 ± 2	4 ± 5	4 ± 2	5 ± 4	9 ± 5	5 ± 3

Table S3. Information on selected SERAC time series for tidewater glaciers. It includes the ID of the glacier used in Fig. 6, figs. S15 and S16 (ID), glacier name (Glacier), drainage basin the glacier belongs to (Basin), ID of the selected SERAC elevation change time series in Fig. 6 (SERAC ID), longitude (SERAC longitude) and latitude (SERAC latitude) of the SERAC time series, surface elevation of the first (Beginning elevation) and last reconstruction (End elevation) in SERAC time series on WGS84 ellipsoid, velocity magnitude from the 1995-2015 velocity mosaic at the location of SERAC time series (Velocity), date of the most retreated terminus position calculated using the terminus position dataset in figs. S15 and S16 along the profile (Date of the most retreated termini), and the distance of the SERAC time series to the most retreated terminus position (SERAC distance to the termini).

ID	Glacier	Basin	SERAC ID	SERAC longitude	SERAC latitude	Beginning elevation (m)	End elevation (m)	Velocity (m/year)	Date of the most retreated termini	SERAC distance to the termini (m)
Fig. S4	Nansem_Gletscher	NW	17000652	-55.266	76.319	1926	1925	52	NA	NA
1	Docker Smith Gletscher W	NW	17002982	-61.896	76.336	339	175	1090	2015-09-12	2101
2	Dietrichson	NW	15000222	-57.936	75.459	291	163	1136	2020-09-03	1234
3	Steenstrup	NW	15003663	-57.766	75.327	426	298	1289	2016-09-05	5781
4	Kakivfaat Sermiat	NW	11002191	-55.275	73.484	276	151	1507	2020-02-19	1520
5 (Jak1)	Jakobshavn Isbrae	CW	5004363	-49.525	69.12	427	226	8539	2021-07-21	788
5 (Jak2)	Jakobshavn Isbrae	CW	5004526	-49.358	69.112	617	410	5854	2021-07-21	7067
5 (Jak3)	Jakobshavn Isbrae	CW	5011810	-49.006	69.145	932	807	2486	2021-07-21	20542
5 (Jak4)	Jakobshavn Isbrae	CW	5003844	-48.766	69.186	1054	950	1802	2021-07-21	30488
5 (Jak5)	Jakobshavn Isbrae	CW	5008153	-48.506	69.206	1225	1146	1183	2021-07-21	41078
6	Zachariae Isstrom	NE	26002976	-21.653	78.901	292	219	735	2020-05-30	13487
7 (Kan1)	Kangerlussuaq	CE	5030019	-33.228	68.751	853	659	1391	2018-11-11	17574
7 (Kan2)	Kangerlussuaq	CE	5030023	-33.048	68.657	518	351	5910	2018-11-11	4734
8	Helheim Gletscher	SE	3001259	-38.389	66.416	563	464	5196	2017-08-23	8677
9	Ikertivaq NN	SE	3007265	-39.674	65.715	444	221	5734	2018-12-26	1531
10	Tingmiarmiut Fjord	SE	1001948	-43.442	62.785	984	884	1623	2020-03-19	11682

Dataset S1 (separate file). Annual_mass_change_basins.xlsx. Time series of drainage basin and ice sheet annual total, surface, and dynamic mass change in Gt of ice/year. The cumulative mass change from this study, which was used for the comparison with GRACE, and the mass change estimation from GRACE, are also included. The cumulative mass changes are normalized to the balance year of 2003, and the unit is Gt of ice.

Dataset S2 (separate file). Uncertainty_annual_mass_change_basins.xlsx. The uncertainty estimations of total (Error of total MB) and dynamic (Error of dynamic MB) mass change for the Greenland Ice Sheet and each drainage basin. It includes two types of uncertainties: 1) Spread of MB: the standard deviation of the three mass change reconstructions using different firn height change datasets, and 2) FE_FDM (where FDM can be IMAU, GSFC, and GEMB): the formally propagated errors described in the Supplementary Text. In addition, the errors of multi-year average mass changes are also available in the sheet named Error of total MB (5 years) and Error of dynamic MB (5 years). The unit of error estimation is Gt of ice/year.

Dataset S3 (separate file). Formal_uncertainty_components_basins.xlsx.The uncertainty components that contribute to the uncertainty estimates of total and dynamic mass change from formal error propagation (FE_FDM in Data S2. Uncertainty_annual_mass_change_basins.xlsx), as described in the Supplementary Text. It includes GIA (GIA), firn air content change error (FAC), firn height change error (FDM_dh), ALPS interpolation error (ALPS_FDM, where FDM can be IMAU, GSFC, and GEMB), and elastic vertical land motion error (ELA_FDM). The unit is Gt of ice/year.

SI References

1. T. Schenk, B. Csatho, A New Methodology for Detecting Ice Sheet Surface Elevation Changes From Laser Altimetry Data. *Ieee Trans. Geosci. Remote Sens.* **50**, 3302–3316 (2012).

2. T. Schenk, B. Csatho, C. van der Veen, D. McCormick, Fusion of multi-sensor surface elevation data for improved characterization of rapidly changing outlet glaciers in Greenland. *Remote Sens. Environ.* **149**, 239–251 (2014).

3. B. M. Csatho, *et al.*, Laser altimetry reveals complex pattern of Greenland Ice Sheet dynamics. *Proc. Natl. Acad. Sci. U. S. A.* **111**, 18478–18483 (2014).

4. J. A. MacGregor, *et al.*, The Scientific Legacy of NASA's Operation IceBridge. *Rev. Geophys.* **59**, e2020RG000712 (2021).

5. H. J. Zwally, *et al.*, ICESat's laser measurements of polar ice, atmosphere, ocean, and land. *J. Geodyn.* **34**, 405–445 (2002).

6. T. Markus, *et al.*, The Ice, Cloud, and land Elevation Satellite-2 (ICESat-2): Science requirements, concept, and implementation. *Remote Sens. Environ.* **190**, 260–273 (2017).

7. N. J. Korsgaard, *et al.*, Digital elevation model and orthophotographs of Greenland based on aerial photographs from 1978-1987. *Sci. Data* **3**, 160032 (2016).

8. G. S. Babonis, B. Csatho, T. Schenk, MASS BALANCE CHANGES AND ICE DYNAMICS OF GREENLAND AND ANTARCTIC ICE SHEETS FROM LASER ALTIMETRY. *Int. Arch. Photogramm. Remote Sens. Spat. Inf. Sci.* **XLI-B8**, 481–487 (2016).

9. R. Forsberg, Greenland (GGEOID16). International Service for the Geoid. Deposited 2016.

10. G. A. Milne, *et al.*, The influence of lateral Earth structure on glacial isostatic adjustment in Greenland. *Geophys. J. Int.* **214**, 1252–1266 (2018).

11. S. Adhikari, *et al.*, Decadal to Centennial Timescale Mantle Viscosity Inferred From Modern Crustal Uplift Rates in Greenland. *Geophys. Res. Lett.* **48**, e2021GL094040 (2021).

12. B. S. Lecavalier, *et al.*, A model of Greenland ice sheet deglaciation constrained by observations of relative sea level and ice extent. *Quat. Sci. Rev.* **102**, 54–84 (2014).

13. S. Adhikari, E. R. Ivins, E. Larour, ISSM-SESAW v1.0: mesh-based computation of gravitationally consistent sea-level and geodetic signatures caused by cryosphere and climate driven mass change. *Geosci. Model Dev.* **9**, 1087–1109 (2016).

14. K. M. Cuffey, W. S. B. Paterson, *The physics of glaciers*, Fourth edition (Elsevier, 2010).

15. M. Brils, P. Kuipers Munneke, W. J. van de Berg, M. van den Broeke, Improved representation of the contemporary Greenland ice sheet firn layer by IMAU-FDM v1.2G. *Geosci. Model Dev.* **15**, 7121–7138 (2022).

16. A. S. Gardner, N.-J. Schlegel, E. Larour, Glacier Energy and Mass Balance (GEMB): a model of firn processes for cryosphere research. *Geosci. Model Dev.* **16**, 2277–2302 (2023).

17. B. Medley, T. A. Neumann, H. J. Zwally, B. E. Smith, C. M. Stevens, Simulations of firn processes over the Greenland and Antarctic ice sheets: 1980–2021. *The Cryosphere* **16**, 3971–4011 (2022).

18. B. Vandecrux, *et al.*, The firn meltwater Retention Model Intercomparison Project (RetMIP): evaluation of nine firn models at four weather station sites on the Greenland ice sheet. *The Cryosphere* **14**, 3785–3810 (2020).

19. X. Fettweis, *et al.*, GrSMBMIP: intercomparison of the modelled 1980–2012 surface mass balance over the Greenland Ice Sheet. *The Cryosphere* **14**, 3935–3958 (2020).

20. B. Noel, W. J. van de Berg, S. Lhermitte, M. R. van den Broeke, Rapid ablation zone expansion amplifies north Greenland mass loss. *Sci. Adv.* **5**, eaaw0123 (2019).

21. R. Gelaro, *et al.*, The Modern-Era Retrospective Analysis for Research and Applications, Version 2 (MERRA-2). *J. Clim.* **30**, 5419–5454 (2017).

22. N.-J. Schlegel, A. Gardner, Output from the Glacier Energy and Mass Balance (GEMB v1.0) forced with 3-hourly ERA5 fields and gridded to 10km, Greenland and Antarctica 1979-2023. Zenodo. https://doi.org/10.5281/ZENODO.10806250. Deposited 11 March 2024.

23. B. Noël, *et al.*, A daily, 1 km resolution data set of downscaled Greenland ice sheet surface mass balance (1958–2015). *The Cryosphere* **10**, 2361–2377 (2016).

24. B. E. Smith, *et al.*, Evaluating Greenland surface-mass-balance and firn-densification data using ICESat-2 altimetry. *The Cryosphere* **17**, 789–808 (2023).

25. P. Shekhar, B. Csatho, T. Schenk, C. Roberts, A. K. Patra, ALPS: A Unified Framework for Modeling Time Series of Land Ice Changes. *Ieee Trans. Geosci. Remote Sens.* **59**, 6466–6481 (2021).

26. P. Rastner, *et al.*, The first complete inventory of the local glaciers and ice caps on Greenland. *The Cryosphere* **6**, 1483–1495 (2012).

27. K. K. Kjeldsen, S. A. Khan, W. T. Colgan, J. A. MacGregor, R. S. Fausto, Time-Varying Ice Sheet Mask: Implications on Ice-Sheet Mass Balance and Crustal Uplift. *J. Geophys. Res. Earth Surf.* **125**, e2020JF005775 (2020).

28. E. Rignot, J. Mouginot, Ice flow in Greenland for the International Polar Year 2008–2009. *Geophys. Res. Lett.* **39** (2012).

29. I. Joughin, D. E. Shean, B. E. Smith, D. Floricioiu, A decade of variability on Jakobshavn Isbrae: ocean temperatures pace speed through influence on melange rigidity. *Cryosphere* **14**, 211–227 (2020).

30. S. B. Luthcke, *et al.*, Antarctica, Greenland and Gulf of Alaska land-ice evolution from an iterated GRACE global mascon solution. *J. Glaciol.* **59**, 613–631 (2013).

31. B. D. Loomis, S. B. Luthcke, T. J. Sabaka, Regularization and error characterization of GRACE mascons. *J. Geod.* **93**, 1381–1398 (2019).

32. S. A. Khan, *et al.*, Accelerating Ice Loss From Peripheral Glaciers in North Greenland. *Geophys. Res. Lett.* **49**, e2022GL098915 (2022).

33. W. Richard Peltier, D. F. Argus, R. Drummond, Comment on “An Assessment of the ICE-6G_C (VM5a) Glacial Isostatic Adjustment Model” by Purcell et al. *J. Geophys. Res. Solid Earth* **123**, 2019–2028 (2018).

34. R. Hugonnet, *et al.*, Uncertainty Analysis of Digital Elevation Models by Spatial Inference From Stable Terrain. *IEEE J. Sel. Top. Appl. Earth Obs. Remote Sens.* **15**, 6456–6472 (2022).

35. N. B. Karlsson, *et al.*, A first constraint on basal melt-water production of the Greenland ice sheet. *Nat. Commun.* **12**, 3461 (2021).

36. I. Joughin, B. Smith, I. Howat, T. Scambos, MEaSUREs Multi-year Greenland Ice Sheet Velocity Mosaic, Version 1. NASA National Snow and Ice Data Center Distributed Active Archive Center. https://doi.org/10.5067/QUA5Q9SVMSJG. Deposited 2016.

37. E. Zhang, G. Catania, D. T. Trugman, AutoTerm: an automated pipeline for glacier terminus extraction using machine learning and a “big data” repository of Greenland glacier termini. *The Cryosphere* **17**, 3485–3503 (2023).

38. S. Goliber, *et al.*, TermPicks: a century of Greenland glacier terminus data for use in scientific and machine learning applications. *The Cryosphere* **16**, 3215–3233 (2022).

39. M. Morlighem, *et al.*, BedMachine v3: Complete Bed Topography and Ocean Bathymetry Mapping of Greenland From Multibeam Echo Sounding Combined With Mass Conservation. *Geophys. Res. Lett.* **44**, 11051–11061 (2017).

40. A. Gardner, M. Fahnestock, T. Scambos, MEaSUREs ITS_LIVE Landsat Image-Pair Glacier and Ice Sheet Surface Velocities, Version 1. NASA National Snow and Ice Data Center Distributed Active Archive Center. https://doi.org/10.5067/IMR9D3PEI28U. Deposited 2022.

41. J. Mouginot, *et al.*, Forty-six years of Greenland Ice Sheet mass balance from 1972 to 2018. *Proc. Natl. Acad. Sci. U. S. A.* **116**, 9239–9244 (2019).

42. B. Vandecrux, *et al.*, Firn data compilation reveals widespread decrease of firn air content in western Greenland. *The Cryosphere* **13**, 845–859 (2019).

43. I. N. Otosaka, *et al.*, Mass balance of the Greenland and Antarctic ice sheets from 1992 to 2020. *Earth Syst. Sci. Data* **15**, 1597–1616 (2023).

44. S. A. Khan, *et al.*, Greenland Mass Trends From Airborne and Satellite Altimetry During 2011–2020. *J. Geophys. Res. Earth Surf.* **127**, e2021JF006505 (2022).

45. S. B. Simonsen, V. R. Barletta, W. T. Colgan, L. S. Sorensen, Greenland Ice Sheet Mass Balance (1992-2020) From Calibrated Radar Altimetry. *Geophys. Res. Lett.* **48**, e2020GL091216 (2021).

46. B. Smith, *et al.*, Pervasive ice sheet mass loss reflects competing ocean and atmosphere processes. *Science* **368**, 1239-+ (2020).